UNIVERSITY OF CALIFORNIA
RIVERSIDE

Tunneling Studies of Superconducting Cuprate with Helium Disordered Barriers

A Dissertation submitted in partial satisfaction
of the requirements for the degree of

Doctor of Philosophy

in

Materials Science and Engineering

by

Yan-Ting Wang

September 2021

Dissertation Committee:

Dr. Shane A. Cybart, Chairperson
Dr. Yongtao Cui
Dr. Peng Wei

The Dissertation of Yan-Ting Wang is approved:

Committee Chairperson

University of California, Riverside

Acknowledgments

First of all, I would like to express my deepest appreciation for my advisor, Prof. Shane Cybart. He guided and taught me his knowledge and shared his experiences with me to direct me to achieve my research goal. He granted me all the access to the equipment that I need for the research projects and also gave me the opportunity to learn every technique I want. I deeply thank him for his patient guidance and unconditional support.

I also want to thank two previous postdoctoral researchers Dr. Ethan Cho and Dr. Hao Li. Ethan taught me the experimental skills and logical thinking with so much patience, and always accompanied me to go through every single detail until I can work independently. Thank you for looking after me. Hao shared a lot of his knowledge to advise me and we had a lot of discussions when I encountered any challenges for my research progress. I would like to express my special gratitude for Prof. Robert Dynes at UC San Diego who shares his valuable suggestions and research experiences with me.

I am very thankful for all my PhD colleagues: Jay LeFebvre, Han Cai, Stephen McCoy, Yuchao Zhou, Anthony Cortez, Miranda Vinay, Joey Forman, and Adhilsha Parachikunnumal. Jay, I enjoy my graduate life a lot with all of our research and nerdy discussions and numerous collaborative works between us. Han, thank you for always standing by my side and encouraging me when I feel unsecured. Stephen, I miss you after you graduated including your little tricks and thank you for teaching me YBCO growth. Yuchao, thank you for always pointing out my problems and trying to help me out when I feel disappointed about myself. Anthony, I always like the moment when we met in the gym and said "cómo estás" to each other. Miranda, you are such a creative person who has good ideas all the

time to pull us together. Thank you for all the manuscripts editing. Joey and Shaz, I learned a lot from you through all the questions you asked. I also want to thank Dr. Dong Yan for his technical training and support. Last, I want to thank all of my roommates for these years, Ethan Cho, Jennifer Cho, Po-Yao Niu, and Suyeon Kang. We have so much fun time that accompanies me through all the challenges I met in pursuing my research goals.

To all my family members for the support. Especially, to my dearest husband, Wei-Hsien Chen, who accompanies me all along with no doubt.

ABSTRACT OF THE DISSERTATION

Tunneling Studies of Superconducting Cuprate with Helium Disordered Barriers

by

Yan-Ting Wang

Doctor of Philosophy, Graduate Program in Materials Science and Engineering
University of California, Riverside, September 2021
Dr. Shane A. Cybart, Chairperson

Quantum computation has aroused many attentions toward the superconducting devices. One of the essential elements is the Josephson junction. This dissertation presents a novel technique for fabricating Josephson junction applying to several superconducting materials using a focused helium ion beam. The fabrication procedure and transport properties of the devices made with different superconducting materials are reported individually.

One of the most well-know high-T_C superconducting cuprate material, $YBa_2Cu_3O_{7-\delta}$, is first implemented with the helium ion technique. Numerous Josephson junctions have been made with $YBa_2Cu_3O_{7-\delta}$ thin films. A deeper analysis for junction characteristics is provided to point out the critical parameters for describing junction behaviors.

The other famous high-T_C cuprate superconductor investigated in this dissertation is $Bi_2Sr_2CaCu_2O_{8+\delta}$ single crystals. I fabricated the first planar Josephson junction on the *a-b* plane of $Bi_2Sr_2CaCu_2O_{8+\delta}$ with helium ion irradiation. The junction orientations are confirmed by the magnetic field measurements, and the nearly perfect Fraunhofer patterns is revealed. This is a breakthrough for development of multidimensional superconducting

circuits.

The mechanisms for cuprate high-T_C superconductivity hasn't been fully understood yet. This work compares the tunneling spectra of the cuprate thin films ($YBa_2Cu_3O_{7-\delta}$) and the cuprate single crystals ($Bi_2Sr_2CaCu_2O_{8+\delta}$). I further study the direct tunneling from a high-T_C cuprate superconductor to another homogeneous high-T_C cuprate superconductor. The spectra reveals tunneling from superconducting carriers and quasi-particles for both materialss. The temperature dependence of the gap-like structures in the spectrum can be depicted with the Bardeen-Cooper-Schrieffer theory, which implies a potential *s*-wave behavior. In contrast, the gapless spectra demonstrate the possible existence of *d*-wave component.

Last, the same technique of high-energy helium ions was employed to irradiate a conventional superconductor, niobium nitride, and a iron-based superconductor. The effects of ion irradiation to these superconducting materials are also presented to assist the potential extension of the technique.

In conclusion, this work provides another perspective to the fundamental mechanism for cuprate high-T_C superconductivity through helium ion disorder barriers with $YBa_2Cu_3O_{7-\delta}$ thin films and $Bi_2Sr_2CaCu_2O_{8+\delta}$ single crystlas. I also established the fabrication procedure for ion disordered *a*-*b* plane Josephson junctions on the fresh cleaved $Bi_2Sr_2CaCu_2O_{8+\delta}$ crystals at any desired angles, which can facilitate the advancement for superconducting circuits. The technique of using helium ion irradiation is further extended to other non-cuprate superconductors and set the footing stone for future applications.

Contents

List of Figures

List of Tables

Chapter 1

Superconductivity

Superconductivity is the phenomena that a drastic reduction of materials occurs in their resistivities when they are cooled down below their transition temperatures. The first superconductor, mercury, was found by Kamerlingh Onnes in 1911. Following the breakthrough discovery, other metallic superconductors such as aluminum and lead were also discovered. It has drawn attention of researchers to study the mechanism behind superconductivity because of its fascinating property of perfect conduction. A lot of theoretical studies started blooming since 1950. The most well-known one is the Bardeen–Cooper–Schrieffer theory which describes superconductivity precisely at an early stage of this field. These models have been well predicting the superconducting characteristics until a different class of superconductors emerged. Explanations for these new found superconductors, with higher transition temperatures in general, are still under debate. In this chapter, We will first discuss the characteristics of superconductivity we observed in our experiments, the fundamental theories that is implemented a lot in our analysis, the essential differences of

categorizations for superconductivity, and a brief cover of overall historical review for the superconducting field.

1.1 Characteristic Phenomena

1.1.1 Perfect Conductivity

The most noticeable property of superconductors is the zero resistances below the critical transition temperatures (T_C). The perfect conductivity makes superconductors the potential material candidates for high power transmission with low energy dissipation. At room temperatures, superconductors can be metals or ceramics. The resistances of non-superconducting metals decrease slowly when cooling down and eventually reach to the lowest non-zero value. In comparison, the resistances of superconductors drop to zero during the transitions. The transition width (ΔT) is defined by two values: (T_C^{onset}) and (T_C^0). The onset point T_C^{onset} is where the reduction of resistance starts to accelerate and also where the transition starts to happen. The value of T_C^0 denotes the material fully enters into its superconducting state at temperatures and the resistance turns into zero absolutely below this point. Narrower transition width (small ΔT) indicates the sharper transition, and usually implies a stronger superconductivity. If the transition is broadened with large ΔT, it usually indicates a weaker superconductor. Therefore, the resistance-temperature measurements provide an effective method to examine superconductivity. Besides, the extrapolation of the normal-state part to the zero-temperature axis is the residual resistance which indicates the amount of defects within the material.

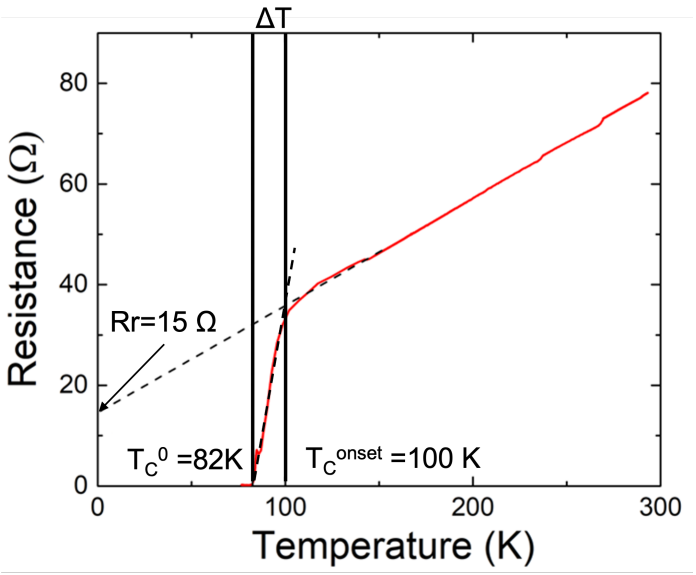

Figure 1.1: The resistance-temperature relation of a superconductor.

1.1.2 Diamagnetism: Meissner Effect

The other important characteristic of superconductors is they demonstrate strong diamagnetism when they transition into the superconducting state. The behavior of expelling magnetic flux further distinguishes the superconductors from perfect conductors. The effect has been massively applied in running the maglev trains. The phenomenon was discovered in the early metallic superconductors, tin and lead, by Meissner and Ochsenfeld in 1933 which is twenty years later after the perfect conductivity of superconductors was observed. The critical field (H_C) is the minimum magnetic field needed to fully destroy superconductivity. Once the applied field is greater than H_C, the magnetic flux can penetrate through the superconductors as they are in the normal state. Some superconductors exhibit two critical boundaries of applied magnetic field in their phase diagram, and thus the superconductors can be categorized into two types.

1.2 Bardeen–Cooper–Schrieffer Theory

The model was proposed by John Bardeen, Leon Cooper, and John Robert Schrieffer in 1952 and known as the BCS theory. It explains conventional superconductivity with a microscopic perspective through the weak couplings between the electrons and phonons. The presumption starts with the following condition: at zero kelvin (T = 0 K), all states below the Fermi level is filled up, and two extra electrons with energy slightly above Fermi energy are added into the system. The two electrons should possess the same-value momentum with opposite directions at the state of lowest energy based on Bloch's theory. An attractive potential between the two electrons is derived and proven to be required for electrons forming the binding state. In other words, conventional superconductivity happens when the two electrons are paired with each other and form a bound-pair state through a weak attracting interaction. The pair is also known as the **Cooper pair**.

The readers may feel confused about the result conflicting with the Coulomb's law that two negative charges should sense repulsion rather than attraction. This is not intuitive if the pairing is considered as the physical connection of two electrons. Instead, it will be easier to understand when picturing them as two separate wave functions overlapping with each together and thus forming a binding wave function as a pair. The attractive potential is not induced by the electrons themselves which are both negative charges. They are paired through the phonon-electron interactions. The vibration of atoms at the crystal lattices stops at T = 0 K, so the electrons are able to move freely among the atoms. When one electron transports through the lattices, the atoms along its path can be attracted by it because they exhibit positive charges based on Coulomb's law. The surrounding atoms

therefore move closer to the electron that just passed by and become a cloud of positive charges, which induces attraction to another electron. Hence, the two electrons are paired together through the interaction with phonons, that is, the perturbation from the movement of atoms at the crystals lattices.

1.3 Categories

Superconductors can be classified into different groups based on their properties. This section helps to differentiate the terms that are commonly used in this field.

1.3.1 Type-I and Type-II Superconductors

The classification of type-I and type-II is based on diamagnetism of superconductors. Superconductivity can be destroyed by magnetic field beyond the critical field of H_C. The type-I superconductor has only one critical value H_C, and therefore it is either in the normal state which allows the magnetic flux to penetrate through or the superconducting state that expels all the magnetic flux. Most metallic superconductors found in the early age are in this classification. The other superconductor of type-II possesses two critical values: the lower critical field (H_{C1}) and the upper critical field (H_{C2}). H_{C1} is the lower boundary where the material transitions from the superconducting state where no flux can penetrate through to the mixed state that only allows quantized vortex existing in the material. As increasing the strength of magnetic field, H_{C2} is the higher boundary where the field is strong enough to fully destroy superconductivity and all magnetic field can go through the material as it is in the normal state.

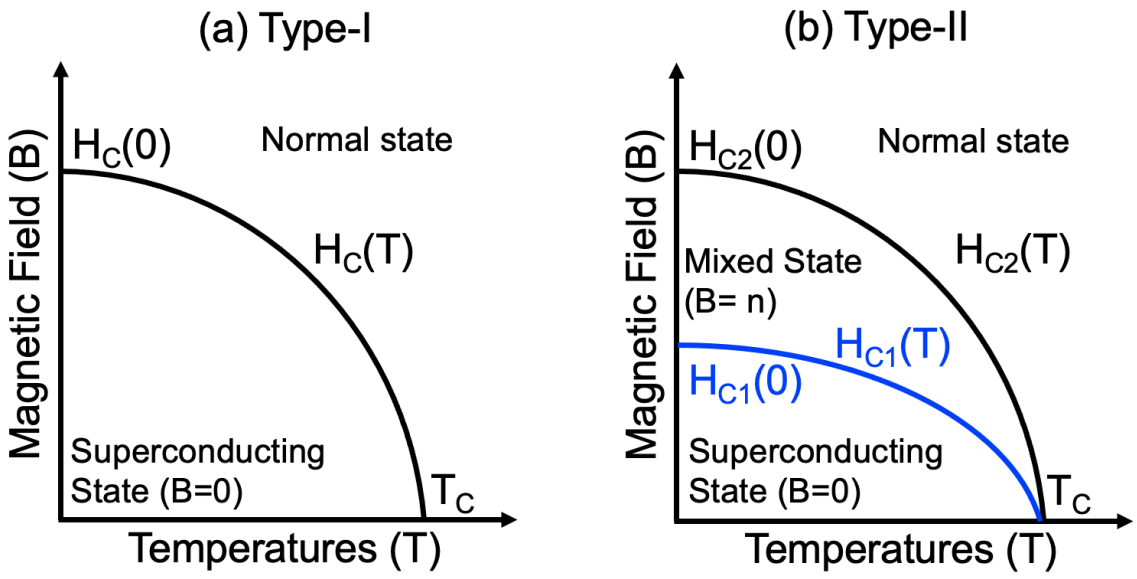

Figure 1.2: The phase diagrams of type-I (a) and type-II superconductors.

1.3.2 Conventional and Unconventional Superconductors

The classification of conventional and unconventional superconductors is judged if its superconductivity can be described by the BCS model with assumption of isotropic *s*-wave superconductivity. The conventional superconductors can be depicted by the BCS model. Most metallic superconductors found in early age fall into the conventional type. However, other superconductors are still under debate that if their mechanism of superconductivity should be explained by the BCS theory. These superconductors are unconventional with gapless quasi-particles excitation spectra instead of obvious gap features with sharp edges. The ceramic copper-oxide superconductors, cuprates, are one of the unconventional superconductors with V-shaped tunneling spectra and high anisotropy.

1.3.3 Low-Transition-Temperature and High-Transition-Temperature Superconductors

The classification of low-transition-temperature (LTS) and high-transition-temperature (HTS) superconductors is based on the values of T_C. The conventional metallic superconductors generally have the transition temperatures below 20 K. Many research groups devoted to seeking new materials with higher T_C. The threshold of T_C for HTS is the liquid nitrogen boiling point 77 K. Most HTS members are the cuprate superconductors at one atmosphere. Recent researches have revealed a superconductor with T_C close to the room temperature under extremely high pressures [3].

1911 First superconductor found by Kamerlingh Onnes
1932 Proximity effect
1933 Meissner Effect
1935 London equation
1950 Macroscopic Ginzburg-Landau theory (type I.)
1952 Abrikosov Vortex
1953 Pippard coherence length
1956 Cooper Pairs
1959 Bardeen-Cooper-Schrieffer Theory (conventional)
1958 Two-fluid model of superconductivity
1959 microscopic Ginzburg-Landau theory (type II.)
1962 Josephson effect (macroscopic quantum theory)
1963 First Josephson junction measured by Anderson and Rowell
1964 Andreev reflection (extension of proximity effect for superconductivity)
1965 Fiske mode
1982 Blonder-Tinkham-Klapwijk model
1986 First high-transition-temperature superconductor found in copper oxide (cuprate) ceramics La-Ba-Cu-O system by Bednorz and Müller
1989 $YBa_2Cu_3O_{7-x}$ with T_C above nitrogen boiling point (77 K) found by Chu and Wu
1988 Bi-Sr-Ca-Cu-O (BSCCO) with T_C above 100 K found by Maeda
1991 Flux focusing effect by Rosenthal
1992 Intrinsic Josephson effects in BSCCO found by Kleiner

Figure 1.3: The history timeline of significant research discoveries in the field of superconductivity

Chapter 2

Josephson Junctions

Josephson effect describes a macroscopic quantum phenomenon that cooper pairs tunneling can happen across a thin insulating regime between two superconductors, and it is predicted by Brian Josephson in 1962 [4]. Josephson junctions are the devices based on the Josephson effect, and they are the fundamental elements in the superconducting circuits, similar with the role of transistors in the semiconducting circuit layouts. They will be massively studied in this work to understand the junction parameters and the tunneling mechanism in different superconducting materials with the technique of a focused helium ion beam. The introduction will start with the configurations and various fabrication methods followed by multiple analysis methods for characterizing junction behaviors, and the current existing applications.

2.1 Josephson Equations

Two superconducting electrodes are linked through a thin barrier, and a supercurrent of cooper pairs can flow across the barrier without voltage drop. Two superconductors have their Ginzburg–Landau wavefunctions Φ_1 and Φ_2 respectively. The phase difference between them is $\Delta\phi$. The amount of supercurrent is determined by $\Delta\phi$ with the maximum value defined as the critical current I_C. The first equation represents the presence of supercurrent without applying voltage and is known as the DC Josephson effect. While maintaining a constant voltage across the barrier, $\Delta\phi$ will change linearly with time and result in an oscillation of supercurrent. The second equation depicts the oscillation known as the AC Josephson effect.

$$I = I_c \sin(\Delta\phi)$$

$$\frac{\partial \Delta\phi}{\partial t} = \frac{2eV}{\hbar}$$

2.2 Geometry and Fabrication

The basic idea of Josephson junctions is to create a barrier between two superconductors. For classic metallic superconductors, it is common to build this configuration with a sandwich-like geometry consisted by superconducting metal-metal oxide-superconducting metal. The tunneling direction of sandwich-type junctions is out-of-plane to the thin films.

The same concept has been applied to HTS thin films as well. The trilayer structures of sandwich-type junctions involve most transport along the c-axis of HTS due to the

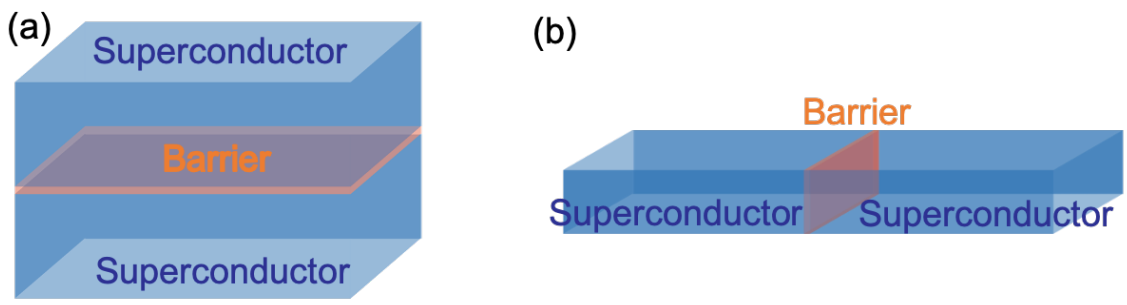

Figure 2.1: The schematic illustrations of (a) a sandwich-type junction with out-of-plane transport and (b) a planar junction with in-plane transport.

geometry. The preferable transport direction has been pointed out to be on the a-b plane for HTS cuprate materials, which is in-plane with the thin films. In order to incorporate the in-plane transport, several researches start to fabricate the planar junctions which have the tunneling barriers with the normal vectors lying on the a-b plane. A thin superconducting wire can be a weak barrier like a weaker superconductor, and it is also known as a Dayem bridge. The step-edge junctions have two superconducting electrodes not on the same plane. The are connected together across a step height between them at a small angle which prevents the discontinuity of the superconducting films caused by abrupt changes in film orientations. The connection usually results a weaker link between the two superconductors in the step-edge junctions. With stronger barriers, the bicrystal grain-boundary junctions and the ramp-edge junction are the most widely used designs for HTS devices with in-plane transport.

Although the Josephson tunneling have been confirmed and the properties have been investigated in these various junctions, the fabrication procedure remains complicated for HTS Josephson junctions. The grain-boundary junctions require HTS films with good quality and locate the grain boundaries precisely to make the devices. For the ramp-

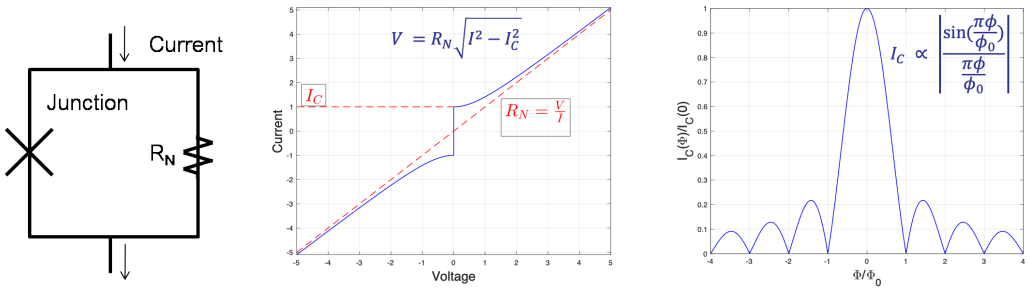

Figure 2.2: Left: the circuit diagram of RSJ model. Middle: the theoretical solution of I-V using a RSJ model. Right: an ideal Fraunhofer pattern formed by I_C responses to the magnetic field.

edge junctions, multiple patterning and milling process and films deposition are needed to fabricate the smooth ramping structures and build the strong barriers along the ramps to maintain transport in-plane with the a-b planes. The author will later introduce a technique that has been revealed recently by Cybart *et al.* [5] to fabricate planar Josephson junctions with the HTS $YBa_2Cu_3O_{7-\delta}$ thin films, and the technique has alleviated the complexity of fabrication procedure for Josephson junctions.

2.3 Junction Characteristics

This section will cover the methods implemented in this work for data analysis. It is important to correctly extrapolate the critical parameters of a junction to understand its behaviors and give the appropriate explanations.

2.3.1 The Resistively Shunted Junction Model

The values of I_C and R_N are the crucial parameters to analyze the junction behaviors. To extrapolate them from the data, the resistively shunted junction (RSJ) model

is employed based on previous theoretical studies [6, 7, 8]. The essential idea is to consider the device as a junction in-parallel with a known resistor (R_N). A simple analytical solution is $V = R_N\sqrt{I^2 - I_C^2}$ as shown in the middle firgure of Fig. 2.2. The coupling strength of two superconductors is related to the value of I_C, and the barrier strength can be expressed by R_N.

2.3.2 Flux Focusing with Rosenthal's Method

The Josephson current can be interfered by a magnetic field with the direction perpendicular to the current direction. The response of I_C values to the magnetic field can form a Fraunhofer diffraction-like pattern with the period of Φ_0 (the right figure of Fig. 2.2) with the following relation.

$$I_C(\Phi_0) = I_C(0)\frac{\sin\frac{\pi\Phi}{\Phi_0}}{\frac{\pi\Phi}{\Phi_0}}$$

Rosenthal *et al.* studied the magnetic interference of the planar Josephson junctions and deducted an equation for the relation between the period of Fraunhofer patterns and the barrier width (w) [9]. The period of one packet in the pattern, except for the central packet, is ΔB which corresponds to one single flux quanta Φ_0. The central maximum peak covers two flux quanta with the period correlates to $2\Phi_0$. The equation is implemented in this dissertation when analyzing the junctions made on the *a*-*b* plane by He-FIB.

$$\Delta B \approx \Phi_0\frac{1.84}{w^2}$$

2.3.3 Excess Current: Andreev Reflection

At an interface between a superconductor and a normal metal, not only Josephson tunneling can happen in carriers transport, but also Andreev reflection, which is the main cause of excess current. The amount of excess current can be extrapolated by extending the linear part at the normal-state range to the zero-voltage axis. This gives a rough estimation of the amount of quasi-particles tunneling and acquires the real value of Josephson tunneling. The ratio of excess current to the total critical current value I_C can be an indication for the strength of barriers. The more portion excess current occupies in the tunneling current, the weaker the barrier is as a normal metal or even a weaker superconductor with suppressed T_C. In the magnetic field measurements, excess current from tunneling of quasi-particles will not respond to the applied magnetic field. Hence, excess current can also be concluded from the variation of I_C values with the magnetic field.

Chapter 3

Techniques Summary

This chapter will summarize all techniques that have been used in each research project. The techniques are divided into four main sections: deposition, fabrication, measurements, and characterization. Deposition includes the methods for putting down the metal layers and growing superconducting thin films. Fabrication introduces the techniques involved in the complete procedure for making devices. Measurements will bring up all different types of experiments that have been conducted to reveal various transport properties of devices. Characterization will mention the tools for obtaining surface morphology and spectroscopic studies. The detailed processing parameters of procedure will only be described here.

3.1 Deposition

Two means are employed to deposit metal layers for the capping layers or the electrical contacts: electron beam (e-beam) evaporation and sputtering. For growth of

superconducting thin films, I only used the sputtering chamber and the AJA system from the oxide nano electronics laboratory (ONELab). The equipment used for metal deposition (Temescal BJD 1800 e-beam evaporator and AJA sputtering system) is provided by the UCR nanofabrication facility.

3.2 Fabrication

Devices for different projects were fabricated with the similar procedure assembled differently by the following techniques. The order of applied techniques will be described again later in each project separately. Here I will present the details including the controlled parameters and the environment.

3.2.1 Exfoliation

The thin-film-like flakes were produced by cleaving the single-crystalline Bi-2212 using Nitto SPV224 tape. From observation of several exfoliation attempts, Nitto tape has less tape residue comparing to conventional scotch tape. The substrate for the flakes was a silicon wafer (100) with a 300-nm thick oxidized layer which varied color contrast of $Bi_2Sr_2CaCu_2O_{8+\delta}$ (Bi-2212) thin flakes with different thicknesses. Considering the penetration depth of the helium ion beam into the Bi-2212 films, the thicknesses of flakes will be roughly estimated from their colors under the optical microscope in this step [10]. This process allowed for a quick selection of viable flakes for further characterization and lithography.

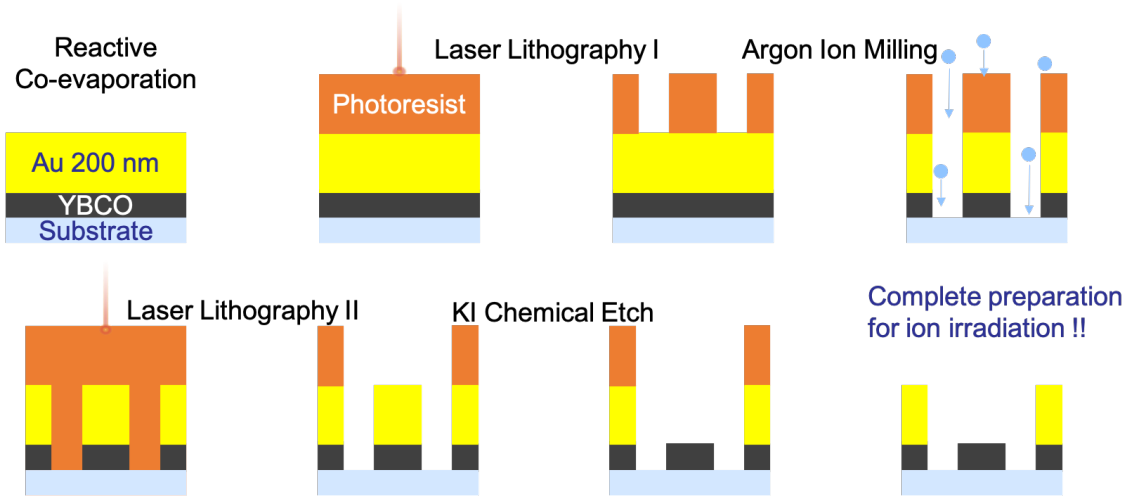

Figure 3.1: The lithography procedure for $YBa_2Cu_3O_{7-\delta}$ (YBCO) thin films in prior to helium ion irradiation

3.2.2 Laser Lithography

The designed patterns are printed on the thin films with conventional lithography. For thin films process, the circuit patterns are transferred by removing extra materials using argon ion milling (Fig. 3.1). For making leads to cleaved single crystals, the contact patterns are formed by depositing a metal layer and leaving the metal into the pattern by lift-off. Lithography is required to print out the patterns on the samples for both thin films and single crystals processing.

The photoresist OCG 825 by Fujifilm was spun onto the samples with rotation rpm 5000 for 45 seconds. Extra solvent can be baked out from the photoresist at 90 °C for 1 minute if needed. The photoresist will become harder if being baked. Baking is not necessary for processing single crystals because the substrates will be heated up during metal sputtering. After spin coating, a g-line laser directly wrote on the photoresist and broke the long chemical chains. The photoresist at the exposed regions by the laser was thus dissolved

by the developer, and the residue solvents were washed away by DI water. Therefore, the circuit patterns need to be inverted to leave the circuit design on the thin films; whereas the contact pattern can be directly drawn by the laser because the photoresist of the pattern needs to be removed for metal deposition. To this step, a temporary mask of photoresist was completed. The mask can be washed away if the resultant pattern is problematic such as electrical shorts by photoresist residue or broken leads from overdeveloping.

Argon Ion Milling for Thin Films

The circuit pattern was printed on the thin film samples after first lithography process. The pattern was transferred into the films by a dry etch technique of argon ion milling. The samples were attached to a bronze stage that will be rotating for uniform etching. The stage was tilted 45° downward to avoid dropping dust onto the sample surfaces during milling. A shutter in front of the stage is closed for 10 seconds in between the milling process of 15 seconds to prevent overheating the films. The total etching time for 30-nm YBCO was tested to be 90∼120 seconds, and around 300 seconds for 200-nm gold (shutter time not included). It is important to check electrical continuity at the spare spaces after ion milling to ensure the YBCO film was etched through without any electrical shorts. After milling, the mask from the first lithography was washed away by acetone. The old photoresist mask at the interested area, where will be irradiate by He-FIB, must be fully removed to etch the gold and avoid any possible surface defects blocking ion irradiation. The samples were thus rinsed by isopropanol to flush extra acetone and dried out by blowing nitrogen gas to the surfaces for second lithography preparation. Second lithography process was used to open the "window" to remove the gold layer at the areas where the helium ion

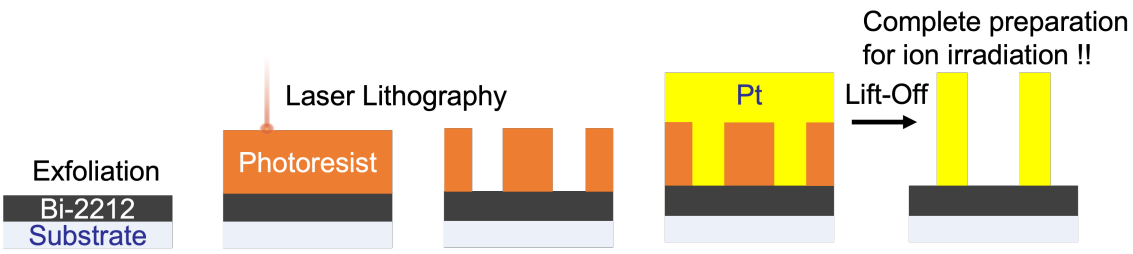

Figure 3.2: The lithography procedure for Bi-2212 exfoliated single crystals in prior to helium ion irradiation

beam will write through because the beam cannot penetrate through 200-nm gold and reach the 35-nm YBCO films. The gold layer at the regions written by the laser was chemically etched by KI, and the extra KI was flushed away by DI water. Use acetone to wash out the photoresist mask from second lithography after confirming the gold was fully etched at the interested areas. The patterned thin films were thus ready for helium ion irradiation.

Lift-off Process for Single Crystals

The processing for single crystals is different from the thin films after first lithography process. The samples were sent to the AJA sputtering chamber without removing the photroresist mask. The platinum layer was directly sputtered onto the samples along with patterned photoresist. After sputtering, the samples were placed in a beaker filled with acetone, and the photoresist was dissolved by acetone in a ultrasonic bath. Only platinum at the areas exposed by the laser was left on the sample surface and thus the contact pads were completed with the lift-off process. The single crystals with patterned contacts were prepared for the next step: helium ion irradiation.

3.2.3 Gallium Focused Ion Beam

The mechanism of gallium focused ion beam (Ga-FIB) is liquid metal ion source. The instrument used in this work is the dual-beam Quanta 200i system in UCR CFAMM. The system consists the primary beam of an electron beam for imaging and the gallium source at the angle of 52° for etching. The two beams need to be precisely aligned at the eucentric point for accurate milling. Ga-FIB is mainly employed to prepare lamella samples for transmission electron microscopy (TEM). Some research studies presented in this dissertation have used Ga-FIB to etch away extra materials that could potentially caused electrical shorts, for example, YBCO residue between bridges from problematic lithography or some fragments of cleaved Bi-2212 crystals between the fabricated contacts.

3.2.4 Helium Ion Microscope

The mechanism of a focused helium ion beam (He-FIB) microscope is gas field ion source. The helium ions were ionized by a sharpened tungsten tip at a high voltage to irradiate the samples. Two He-FIB microscopes by Zeiss were involved in the studies: Orion Plus and NanoFab. The procedure can be divided into three main steps: trimmer forming, beam tuning, and ion irradiation.

Trimmer Forming

The tip temperature is maintained at 80 K by liquid nitrogen with the dewar temperature around 55 K. The trimmer source is first formed at the end of tip by the automatic process. Generally, maintaining or increasing best image voltage (BIV) is selected in this step. Decreasing BIV is only selected if the last trimmer was formed at too high of

voltages (> 45 kV). The trimmer source is appeared as a hexagonal-like crystal structure. The crystal layers can be peeled off by bringing up the extraction voltage. The extraction voltage has a maximum at 50 kV and is kept larger than the acceleration voltage and less than two times of acceleration voltage ($V_{extraction}$ 50 kV, $V_{acceleration} < V_{extraction} < 2V_{acceleration}$). Therefore, one can first raise the acceleration voltage close to 25 kV and start increasing the extraction voltage. The BIV of a trimmer is lower than the forming voltage. For example, if a trimmer is formed at 25 kV, it is less likely to have BIV above 20 kV for this trimmer. This inhibits the system from applying the acceleration voltage higher than 20 kV to accelerate the helium ions for irradiation. Hence, an ideal trimmer is anticipated to be formed within the extraction voltage range of 35∼45 kV so that its BIV can fall within 25∼35 kV. It is important to slow down the raising speed when the extraction voltage is within the range where a trimmer is likely formed. The view of source becomes blurred at high voltages, and only subtle changes in brightness and contrast can be discerned as an indication of a new formed trimmer. Bring down the extraction voltage way lower than the voltage where the subtle change was observed to prevent the loss of a trimmer since three atoms at the tip apex is extremely unstable and may be peeled off quickly at such a high voltage. Once the trimmer is formed, its BIV can be determined by slightly sweeping the voltage to find the brightest spot.

Following the formation of a trimmer, the trimmer alignment for tilt and shift is done mechanically and electrically. The air table needs to be initiated when adjusting the tilt mechanically. Pick an atom of the trimmer, usually the brightest one, and observe its positions in both of the upright and inverted images (above and below the focal plane) by

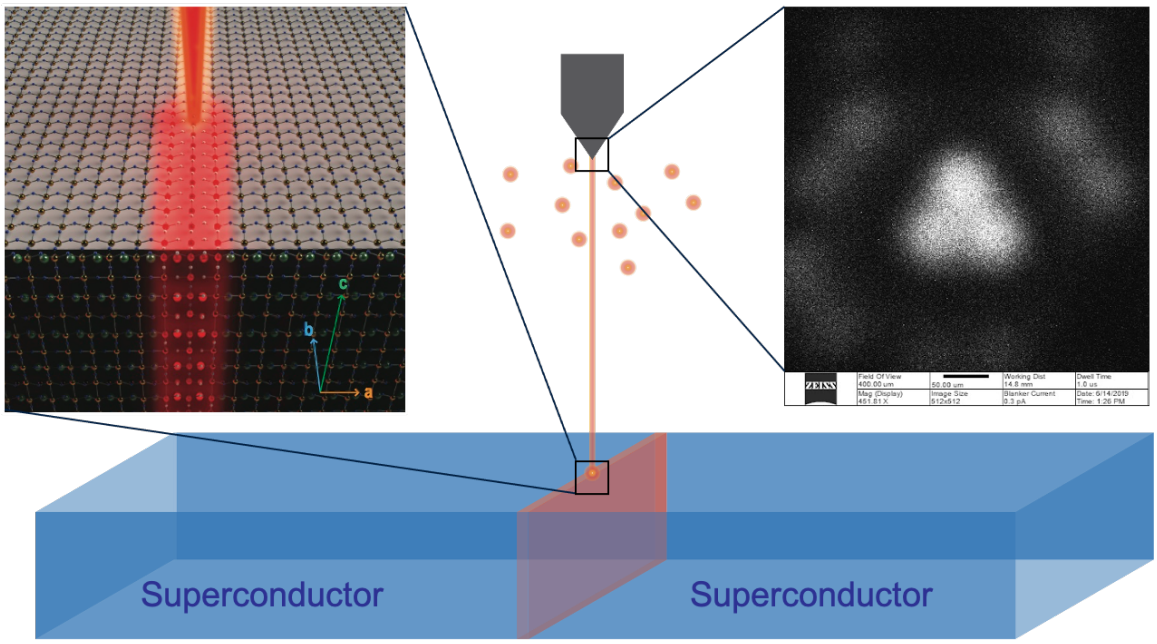

Figure 3.3: The schematic illustration for the mechanism of a focused helium ion beam with a zoom-in view of disordered region (image credited to Dr. Yuchao Zhou) and a screenshot of a trimmer.

sweeping the lens1 voltage. Adjust its position using the mechanical tilt knobs to make both positions at the same spot in the screen. Once the positions of the same atom overlay in both the upright and inverted images, turn off the air table. Choose the aligned the aperture (usually 5 μm) and focus at the aperture. Start driving the beam using the mechanical shift knobs to place the beam, appeared as a bright circle, at the center. The distance between the center and the beam should be less than the radius of the bright spot. The shift can be tuned subtly using electrical tilt once the center falls within the circle when both mechanical knobs are in loosen status. Focus at the edge of aperture to ensure the beam is finely tuned and set the source distance automatically. To reach 0.5 pA, the average helium pressure is around 10^{-6} torr. The trimmer is now ready for general operation. The current value is a crucial parameter to tell if the atom of the trimmer is aligned well (low current if the beam

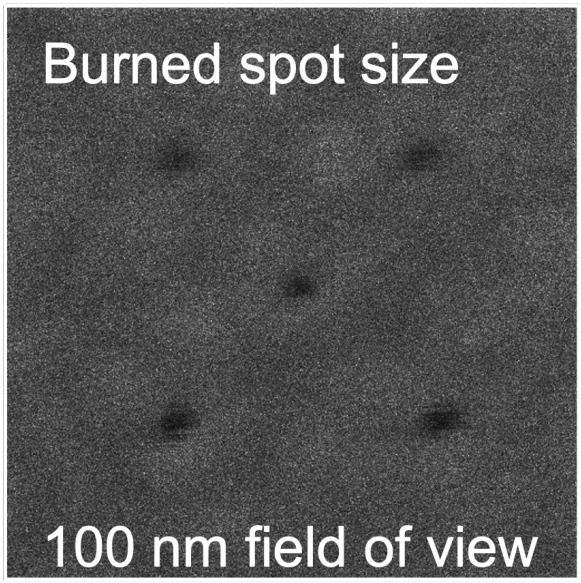

Figure 3.4: Circular spots burned by a optimally tune helium ion beam.

is drifted away from the center).

Beam Tuning

The ion beam is optimized on top of the metal contacts or the reference graphite TEM grids. Three adjustments are needed to obtain the optimum beam: focus, beam shift (wobbling), and stigmation. The working distance for the sample surfaces is around 8 to 9 mm with z-height set as 4 mm. Beam shift needs to be adjusted to reduce wobbling effects when the field of view is shifting when adjusting focus. Stigmation problems exist if scratched patterns are visible when the sample is off focus. Tuning stigmation visually is easier at the rough aluminum wire bonds because there are more features to observe. When on a smooth metal surface, stigmation can be improved by observing the uniformity

of burned spots. Beam stigmation can be finely adjusted by burning elliptical spots to circular spots under field of view of 100 nm.

Ion Irradiation

The beam acceleration voltage was set to be 25 to 30 keV and focused to a beam diameter of 0.5 nm based on previous tuning procedure with the 5-μm aperture. The current is usually controlled to be around 0.5 pA. If the current is too low, increase helium gas pressure, and vice versa. The spacing is set as the same with the ideal beam diameter of 0.5 nm with dwell time 1.0 μs. The ion beam was normal to the surfaces of the target samples, and irradiated the samples without etching any materials. The crystal structure was disordered at the region where the helium ions penetrated, and the material properties was altered. For materials that undergo a superconductor-insulator-transition with disorder, the properties of the barrier can be tuned to a weaker superconductor, a normal metal, or an insulator depending on the ion dose used.

3.3 Measurements

Transport properties are revealed through various measurements. The setup for each type of measurements will be introduced in this section. The resisitivity-temperature (R-T) relations show superconductivity transition of the materials. The current-voltage (I-V) characteristics present the behaviors of Josephson junctions. The voltage responses to the magnetic field (V-B) can evaluate the performances of devices. The changes of critical currents with the applied magnetic field (I_C-B) could be another evidence for Josephson

junctions. The differential conductances (dI/dV) are measured in a wide voltage range to investigate the gap-like structures in the density of states of superconductors.

- Resistivity-Temperature (R-T)
- Current-Voltage (I-V)
- Critical Current-Magnetic Field (I_C-B)
- Differential Conductances (dI/dV)

3.4 Characterization

This section includes the methods for surface studies and element analysis. I studied the topography of the fabricated samples with the atomic force microscope (AFM), the helium ion microscope (HIM), and the scanning electron microscope (SEM). The spectroscopic methods could provide both qualitative and quantitative analysis with energy-dispersive X-ray spectroscopy (EDS/EDX), Raman spectroscopy, and X-ray Diffraction (XRD).

3.4.1 Atomic Force Microscope (AFM)

Atomic force microscopy (AFM) is often used to acquire sample topography when determining the surface roughness and the bubbling effects of helium ions. The aluminum tips used in the experiments are the commercial probes from Bruker. The instrument is a complex system consisted by HORIBA LABRAM and AIST-NT AFM from UCR optical lab.

3.4.2 Scanning Electron Microscope (SEM)

The scanning electron microscopy (SEM) and microanalysis was performed on a the ThermoFisher Scientific (formerly FEI/Philips) Quanta™ 3D 200i and NNS450 in CFAMM at UC Riverside. SEM was used massively in the early state for cuprate single crystals fabrication. The damage from high-dose helium ions can be clearly seen on the surface of the materials and the substrates underneath. SEM is very helpful to root the failure reasons and improve the process.

3.4.3 Spectroscopic Methods

I have employed energy-dispersive x-ray spectroscopy (EDS/EDX) to study the surface defects formed after oxygen annealing the cleaved crystals. X-ray diffraction (XRD) was utilized to examine single crystallinity of Bi-2212. Raman spectroscopy is massively used to determine the number of graphene layers after exfoliation, and I have attempted to try to study Bi-2212 layers with Raman spectroscopy.

Chapter 4

He-FIB Junctions with High-T_C Superconducting Thin Films

First high-transition-temperature superconductor (HTS) was discovered by J. G. Bednorz and K. A. Müller with a copper-oxide ceramic system of La-Ba-Cu-O in 1986. The T_C was found to be around 30 K which is relatively higher than conventional superconductors whose T_C is about 10 K generally. Although the T_C of first HTS is not as much higher as expected, the discovery predicts the debuts of potential HTS in the complex oxides, and intrigues more interest in pursuing higher T_C in the cuprate family. Following this discovery, a breakthrough for HTS materials happened. A superconductor, $YBa_2Cu_3O_{7-\delta}$ (YBCO) was subsequently reported to have T_C at 93 K which is above boiling point of nitrogen 77 K by Wu *et al.* [11].

4.1 $YBa_2Cu_3O_{7-\delta}$

The crystal structure of $YBa_2Cu_3O_{7-\delta}$ (YBCO) is distorted orthorhombic perovskite with the composition of ABO_3. The lattice constants of YBCO are a = 3.82 Å, b = 3.89 Å, and c = 11.68 Å[12]. The unit cell appears to be anisotropic between the a-b plane and c-axis. The similar anisotropy is also observed in the transport properties of YBCO. In the noraml state, YBCO has the lowest resistivity along the **b**-axis parallel to the copper-oxide chains and the largest resistivity along the c-axis. The resisticity is measured to be lower in-plane with the a-b plane than the out-of-plane direction along the c-axis because the copper-oxide planes are on the a-b planes. Superconductivity of cuprate superconductors is from the carriers transport by oxygen vacancies on the copper-oxide planes with the chains as the potential reservoir. Therefore, the oxygen content in the structure can significantly affect superconductivity of cuprates. YBCO, a member of cuprate superconductors, is also sensitive to oxygen concentration.

4.2 Growth Methods

The YBCO thin films studied in this chapter are mainly from two sources. One is the commercial films from Ceraco Ceramics Coating GmbH in Germany grown by reactive co-evaporation (RCE), and the other one is deposited by RF sputtering.

4.2.1 Reactive Co-Evaporation

Reactive co-evaporation (RCE) is a commercial technique for high quality thin films deposition. Substrates are attached to a plate with rotation frequency of 5 Hz, and

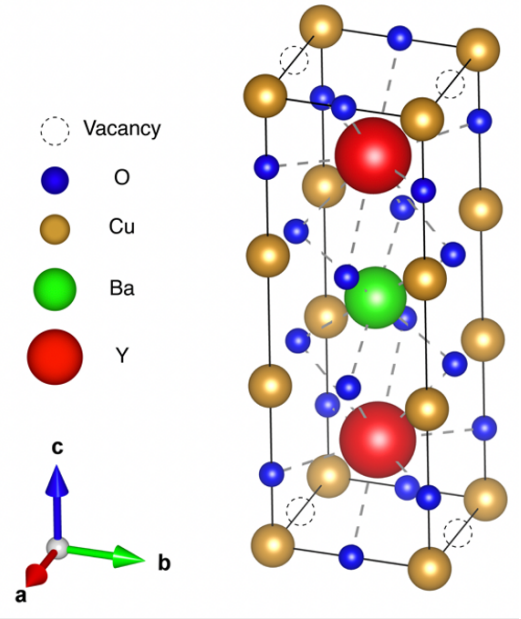

Figure 4.1: The unit cell of YBCO

thus are revolving between the main evaporation chamber and the oxygen "pocket". The evaporation chamber is maintained vacuum at lower pressure of 7.5×10^6 torr, and the metallic elements of yttrium, barium, and copper are thermally evaporated from the resistive sources onto the substrates for YBCO deposition. The oxygen pocket is a black-body heater filled with oxygen gas at a higher pressure of 7.5×10^4 torr. The quartz crystal micro balances with collimators is used to inspect the evaporation rate of the metal sources to maintain the accuracy within 1%. The temperature is one of the critical growth conditions. In RCE process, the growth temperature is at 650 °C, which is almost 150 degrees lower than other deposition techniques. The lower temperature benefits in preventing films cracking down during the cooling process and also avoiding the formation of inter-metallic phases as $BaCeO_3$ for example.

RCE have been routinely producing in large numbers of HTS coated substrates for commercial purposes. The stoichiometric composition is controlled precisely, and the smoothness of these ultra thin films with thickness of the order of a few tens of nanometers meets the grade for electronics applications. As another noticeable advantages of RCE, it has very large deposition area and its rotating oxygen pocket heater further facilitates for a large-size substrate or large number of wafers simultaneously.

4.2.2 RF Sputtering

Our group also grows YBCO thin films on our own using RF off-axis sputtering [13]. The films properties are strongly dependent with the conditions during deposition such as temperatures, pressures, gas flow rate (sccm), argon and oxygen gas ration, annealing time and temperatures, and the distance from the substrates to the target sources. I studied the surfaces of YBCO films at different positions of the rotating plate. The films located at the nearest spot to the YBCO target has has a rougher surface with root mean square (rms) roughness around 15 nm. The substrate placed further from the target has smoother surface with smaller rms around 10 nm. From Fig. 4.2, the grainy structures on the surfaces are clearly seen. Each grain has its own phase, and its a-axis and b-axis do not align to other grains. The grain boundary and lattice mismatch are the main concern for uniform junctions fabrication and tunneling spectra studies.

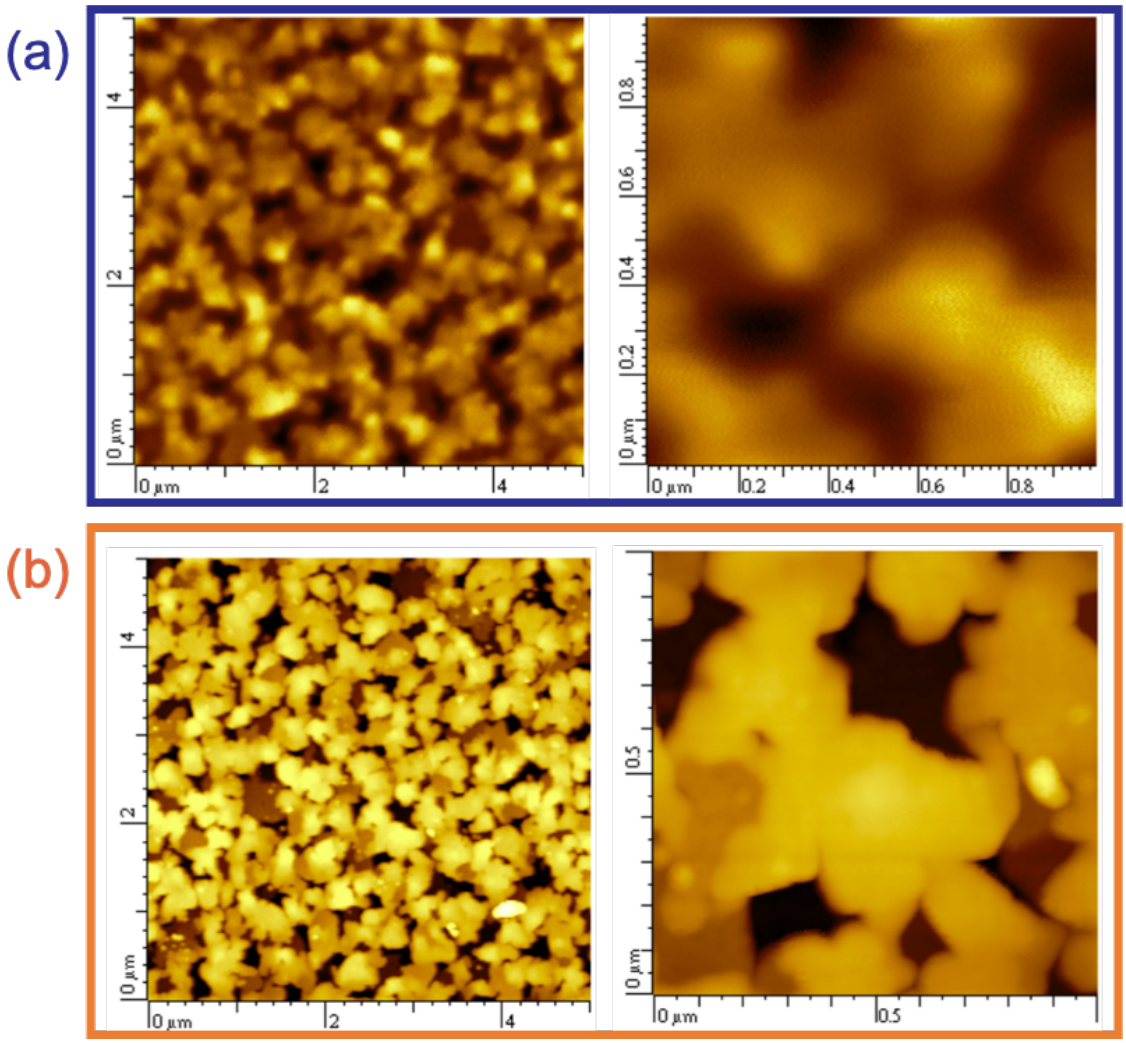

Figure 4.2: The same batch of YBCO films grown by RF sputtering with substrates pacing (a) closest to the target with rms = 15 nm and (b) furthest from the target with rms = 10 nm.

4.3 Multilayers for HTS Ground Planes

This section has been published in 2019 [14]. A multilayer heterostructure consisting of 35-nm YBCO, 75-nm CeO_2, 150-nm YBCO and 20-nm CeO_2 (top to bottom) on r-plane sapphire was grown at Ceraco GmbH using RCE. In the hetreostructures, the layer thicknesses were chosen to be optimized for Josephson devices fabrication using the He-FIB process in the top layer. To create a uniform disordered barrier with He-FIB, it is important to control the film thickness under the penetration depth of helium ions with acceleration voltage around 25 to 30 kV. High quality nanoscale devices can be created with He-FIB, but they require very smooth and thin films with thickness around 35 nm.

The bottom YBCO layer, which served as a ground plane, was designed to have thickness of the same order of the penetration depth of YBCO to ensure the secured shielding ability. As for the insulating layer to separte the device layer and the ground plane, the thickness of CeO_2 layer is maximized as thick as possible while maintaining the total thickness of the multilayer heterostructures under 300 nm to prevent cracking, which is common in films grown on sapphire.

Five 2" r-plane sapphire wafers were placed around the center of the plate(n) for deposition for the multilayer heterostructures used in this section. First a 20-nm buffer CeO_2 layer was grown as the buffer layer to reduce the possibility of lattice mismatches with substrates for the next grown 150-nm thick YBCO film as the bottom ground plane. Smooth films are required to prevent pinhole shorts through the subsequent layers. Hence, the copper content was reduced to eliminate copper-oxide precipitates on the surface at the expense of a reduced T_C and J_C. Second, a 75-nm CeO_2 layer was deposited, and the T_C

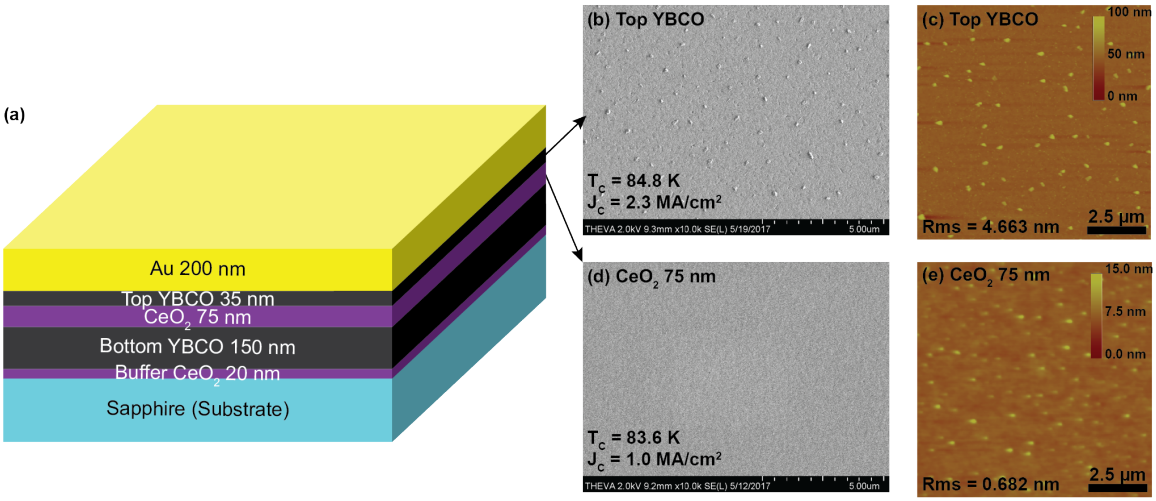

Figure 4.3: (a) Schematic illustration of the multilayer structure consisted with 200-nm Au, 35-nm top YBCO, 75-nm CeO_2, 150-nm bottom YBCO and 20-nm CeO_2 buffer layer on sapphire substrate. (b) The surface topography of 35-nm top YBCO and (d) 75-nm CeO_2 scanned by SEM. (c)The surface topography of 35-nm top YBCO and (e) 75-nm CeO_2 scanned by AFM.

and J_C of the bottom YBCO were measured to be 83.6 K and 1.0 MA/cm^2 respectively using an inductive Cryoscan.

The wafers coated with the bottom 150-nm YBCO and the 75-nm CeO_2 layers were returned to the evaporation vacuum chamber along with an additional CeO_2 buffered sapphire test substrate. A 35-nm thick YBCO layer was grown followed by a 200-nm gold contact layer. For this deposition the copper content was increased to obtain better electrical properties. The 35-nm YBCO layer from this second deposition were measured to have T_C at 84.8 K and J_C of 2.3 MA/cm^2 using a cryoscan of the extra test substrate. A third cryoscan of the heterostructure exhibited a value of J_C around 1.2 MA/cm^2 for the whole stack of thin films (150 nm YBCO/75 nm CeO_2/35 nm YBCO). The bottom 150-nm YBCO layer was measured to have a J_C of 1.0 MA/cm^2 from the first cryoscan; The top

35-nm YBCO layer was estimated to have a J_C of 2.3 MA/cm^2 from the second cryoscan of the test sample. The current density of the whole structure with these two layers can be calculated as 1.25 MA/cm^2 by the weight ratio: (1.0 MA/cm^2 $\times$ 150 nm + 2.3 MA/cm^2 $\times$ 35 nm)/185 nm = 1.25 MA/cm^2. The approximation is consistent with the measured value 1.2 MA/cm^2 of the stack. This suggests that the quality of the 35-nm YBCO on top of the CeO_2/YBCO is similar to the YBCO film on the test substrate.

Atomic force microscopy (AFM) was used to inspect the surfaces to characterize the surface morphology. To scan the surface of the top 35-nm YBCO layer, the gold capping layer was chemically removed with KI-I^+ gold etch. The surface topography of the 75-nm CeO_2 insulating layer was acquired by removing the top YBCO by phosphoric acid of some multilayer samples or from other test samples taken out from the evaporation chamber after the 75-nm CeO_2 deposition. Both the YBCO top layer and CeO_2 surfaces were smooth with the exception of a small number of particles on the top of YBCO surface as shown in Fig. 4.3. Large scale defects or cracks were not observed. Surface roughness was determined to be 0.7 nm and 4.7 nm for the CeO_2 and top 35-nm YBCO respectively.

Resistivity as a function of temperature (R-T) was measured for both YBCO layers using a four-point Van der Pauw geometry and lock-in amplifiers to examine their superconducting transitions. The results are shown in Fig. 4.4. To access only the bottom 150-nm YBCO layer for this measurement, the top YBCO layer was fully removed with phosphoric acid and the insulating CeO_2 layer was scribed through with a diamond cutter to make contact with the bottom YBCO layer.

Both YBCO layers exhibit sharp transitions with the residual resistivities of 22

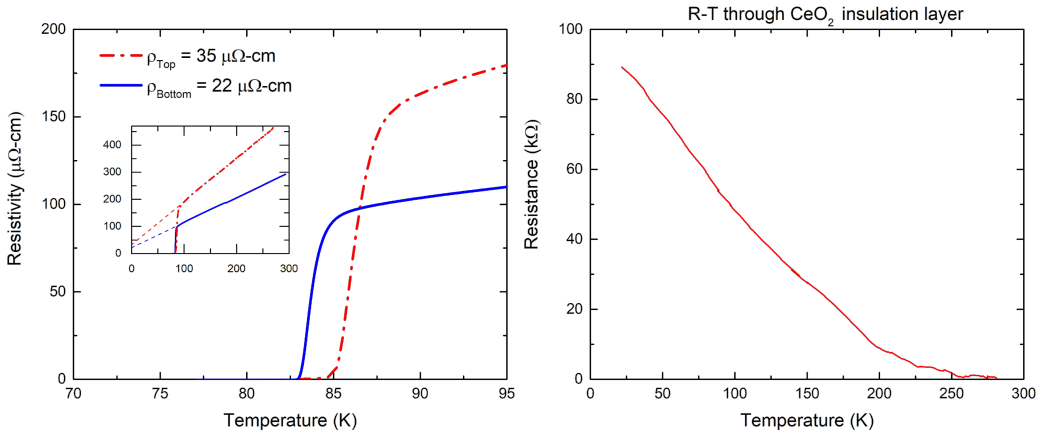

Figure 4.4: R-T measurements of top 35-nm YBCO and bottom 150-nm YBCO (left) and middle insulating 75-nm CeO_2 layer (right) individually

$\mu\Omega$-cm and 35 $\mu\Omega$-cm for the top and bottom layers respectively, which suggests that there is small temperature independent defect scattering. The top 35-nm YBCO shows an apparent room temperature resistivity of 500 $\mu\Omega$-cm which is much higher than the bottom 150-nm YBCO layer with resitivity of 275 $\mu\Omega$-cm at room temperature. The result is interpreted as an overestimate of the electrical thickness of the top layer. Processing damage, surface roughness and a possible dead layer at the interface between the top 35-nm YBCO and 75-nm CeO_2 are likely the reasons contributing to a reduction of the electrical thickness of the top YBCO layer. Assuming that the actual resistivity of the two layers is the same yields a reasonable electrical thickness of 20 nm for the top YBCO layer.

The electrical properties of the CeO_2 insulating layer needs to be characterized to examine the presence of pinhole shorts. The R-T measurement of CeO_2 was performed with a four-terminal configuration from the top to the bottom YBCO layer. In order to make proper electrical contact with the buried YBCO, a 3-mm diameter circle was printed on

top of the sample using a drop of photoresist. The circle pattern was transferred into both gold and the top YBCO layer by chemical etching with KI-I+ and 0.1% phosphoric acid respectively. The CeO_2 layer was thus etched using a 500-V argon ion mill. To ensure the CeO_2 layer was totally milled through and the bottom YBCO layer was exposed, electrical continuity was tested between the bottom contacts and the etch step height of the milling step between the circle pattern and the milled surface was measured to be 320 nm with a KLA Tencor P-7 profilometer. I first measured R-T across the CeO_2 layer by flowing the current from the top YBCO layer to the bottom YBCO layer. The result revealed that the insulation of the CeO_2 layer grew stronger at low temperatures. To fully examine its insulating property, a set of I-V measurements across the CeO_2 layer was done at different temperatures, and R-T results was extrapolated from the I-V with various bias voltages.

Two electrical contacts were attached to the top gold electrode of the patterned 3-mm circle. The other two were attached to the exposed bottom YBCO layer by argon ion milling process with silver paint. Current as a function of voltage (I-V) was measured by using an arbitrary function generator to drive the current source across the sample and the series resistor at 1 Hz. Low noise pre-amplifiers were used to measure the voltage across the CeO_2 (V) and the current across the series resistor (I). The I-V curves were continuously recorded and the sample was cooled to low temperature using cryogenics. Selected curves are shown in Fig. 4.5(a) measured at a series of different temperatures. At room temperature, the insulating CeO_2 layer appeared to be ohmic with a resistance of 351 Ω. However as temperature was reduced below 200 K, non-linearity started to be observable (Fig. 4.5 (a)).

To investigate the temperature dependence further, the resistivity was calculated

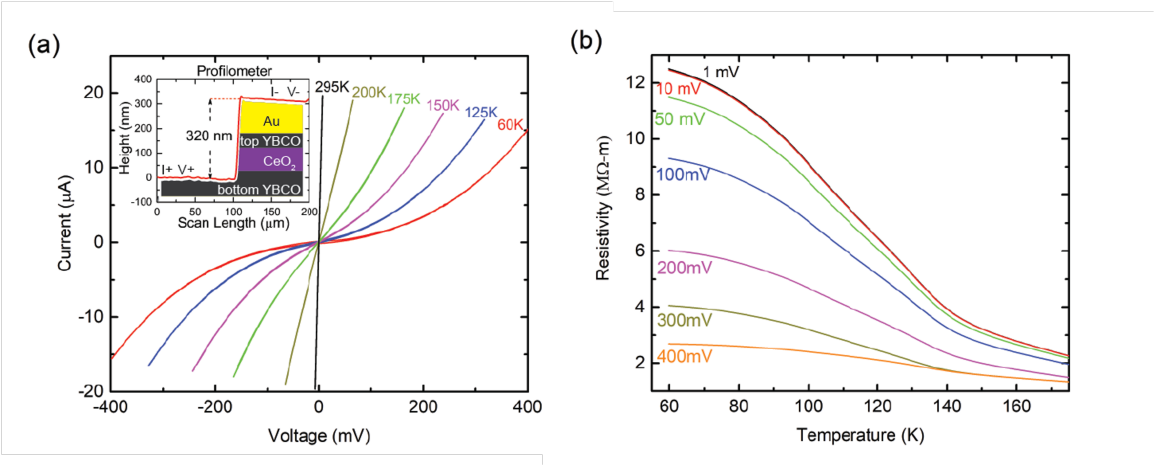

Figure 4.5: (a) Current-Voltage across 75-nm CeO_2 insulating layer measured at different temperatures. The inset is the step height obtained by the profilometer to ensure etching was through the layers. (b) Resistivity-Temperature of 75-nm CeO_2 insulating layer obtained from (a) for different constant voltage ranges.

assuming the uniform current density through the patterned area from the resistance obtained from the data in Fig. 4.5 (a). The result was plotted for several ranges of biased voltage in Fig. 4.5 (b). A strong dependence of the resistivity on both temperature and voltage was observed, which is reminiscent with variable range hopping transport. The appearance of the data approaches an asymptotic value at low temperature, and this is likely an artifact from using a measurement voltage much greater than the thermal energy k_BT. From these large area measurements of I-V and R-T, two conclusions are drawn that there are no pinhole shorts through the dielectric and that the transport mechanism is thermally activated variable range hopping.

In this section, superconducting YBCO-CeO_2-YBCO thin films in multilayer heterostructures grown by RCE were investigated through surface and electrical characterizations. The top 35-nm and the bottom 150-nm YBCO layers both exhibited high T_C values

at 83.6 K and 84.8 K and large critical current density with moderate surface roughness. The CeO_2 insulator demonstrates activated transport but provides more substantial insulation with high resistivty of 11.5 MΩ-m at 77 K. Additional structural characterization such as x-ray diffraction and transmission electron microscopy could potentially yield more insight into the quality of these structures. In terms of electrical properties, these films appear very suitable for high-T_C thin film electronics. This is a step further walking towards a large scale commercial multilayer RCE process for HTS electronics. The incorporation of interconnecting vias and crossovers is envisioned for more complex integrated HTS circuits.

4.4 YBCO *a-b* plane Junctions

The same fabrication procedure introduced in chapter 3 was applied to the commercial YBCO films to make numerous circuit patterns. To study the junction parameters, the design of YBCO twenty bridges (the left picture in Fig. 4.6) was used a lot to test the ion dose. Before processing, the ion disordered level of YBCO can be simulated with SRIM [15]. The scale of right images of Fig. 4.6 is comparable, and the difference of disordered range can be clearly seen. The masked ion irradiation has a broader disordered region while the range is much narrower if a focused beam is used instead.

While studying the different ion doses, the barrier strength is found to be strongly related to the disordered level. The barrier exhibits higher strength with higher diordered level. The heavier ion dose results in a more insulating barrier. The metal-insulator transition is observed in the He-FIB junctions of YBCO films by controlling ion doses.

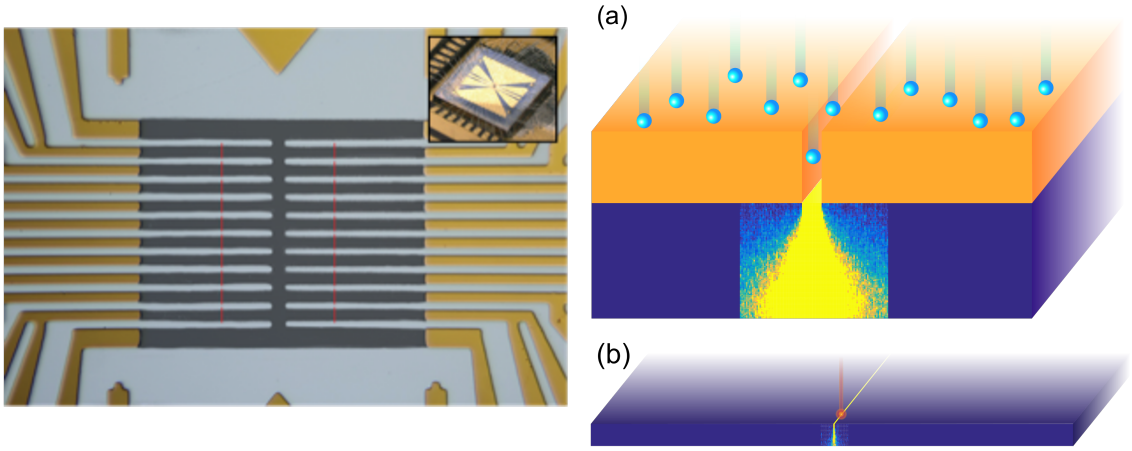

Figure 4.6: Left: an optical image of a 20 bridge YBCO sample. Right: (a) SRIM results of ion disorder level of YBCO using a mask. (b): SRIM results of ion disorder level of YBCO using direct writing with a focused helium ion beam

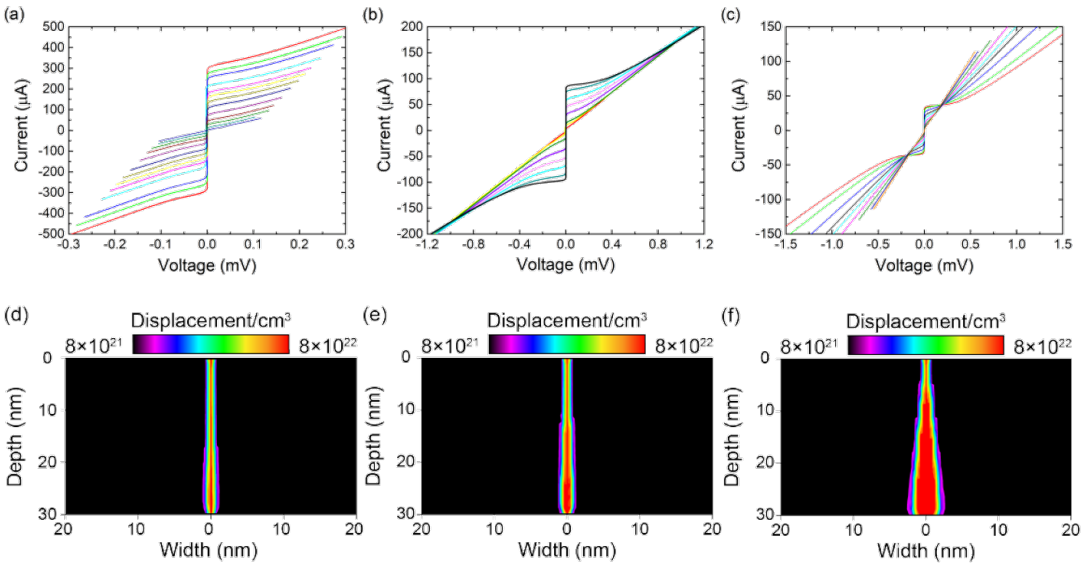

Figure 4.7: The barriers of YBCO He-FIB junctions as (a) a normal metal, (b) in the middle of transition, (c) an insulator. (d-f) The disordered level of YBCO corresponded to (a), (b), and (c).

Chapter 5

He-FIB Junctions with High-T_C Superconducting Single Crystals

This chapter covers the content of using He-FIB to fabricate Josephson junctions on the widely studied HTS single crystals, $Bi_2Sr_2CaCu_2O_{8+\delta}$ (Bi-2212). The junction characteristics of Bi-2212 He-FIB junctions share the same metal-insulator transition with the YBCO He-FIB junctions by different helium ion doses. Studying the controllable Bi-2212 He-FIB junctions on its a-b plane is helpful to develop multidimensional superconducting circuit designs combing with the intrinsic Josephson junctions along its c-axis. We first start with the introduction of the material properties, how we processed and measured the samples, and the last part about analysis of our results.

5.1 Introduction

Cuprate HTS single crystals possess high uniformity with less disorder in the materials comparing with thin films. Since cuprate superconductors are generally sensitive to the amount of disorder in the crystal structures, the single crystals with high quality can thus provide a platform to study the superconducting mechanisms behind cuprate HTS excluding the effects from non-uniformity. Single-crystalline HTS may also be beneficial to fabricate He-FIB junctions with more stable performances and less ion doses deviations. In this dissertation, $Bi_2Sr_2CaCu_2O_{8+\delta}$ is chosen as the target material for investigating helium ion disordered Josephson junction properties and compared with the results of YBCO.

5.1.1 Discovery of Bi-Sr-Ca-Cu-O System

Bismuth strontium calcium copper oxide system (Bi-Sr-Ca-Cu-O, BSCCO) is found as the first HTS without a rare earth element by Maeda et al. in 1988 [16]. They observed the crystals transitioned into a diamagnetic state around the same temperatures where the sudden dropped resistivity occurred, and thus confirmed its T_C to be around 75 K at which the resistivity turned into zero completely. The group also noticed that the presence of calcium and the ratio of copper elements in the composition significantly affect T_C values of the crystals. The absence of calcium in the crystals ($Bi_2Sr_2CuO_{6+\delta}$, Bi-2201) were found to have the lowest T_C below 30 K [17] among the members in BSCCO family.

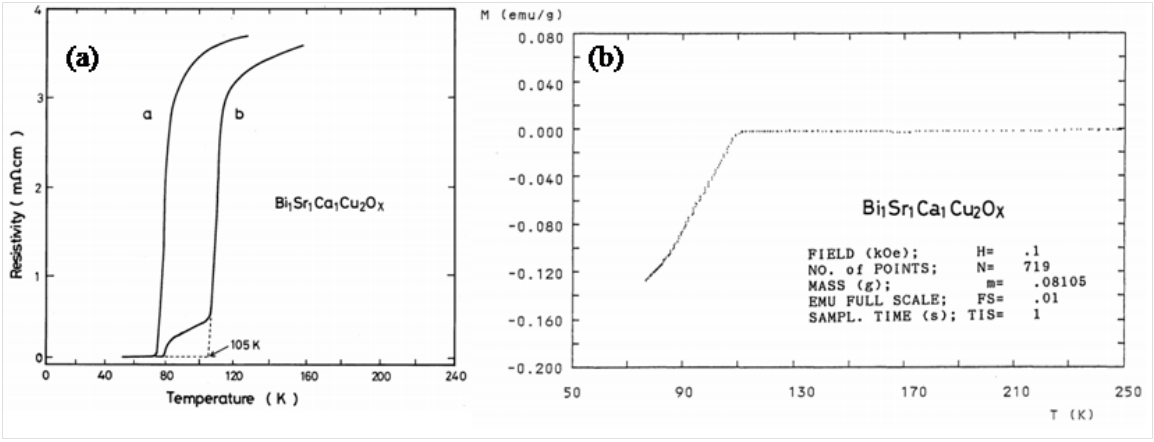

Figure 5.1: (a) The resistivities versus temperature of two BSCCO crystals grown in different conditions. Crystal **a** was grown at 800 °C for 8 hours, while crystal **b** was grown at 882 °C for 20 minutes with post-annealing at 872 °C for 9 hours. (b) The magnetization level versus temperature of BSCCO crystal **b** in an 100-Oe field.

5.1.2 Bi-Sr-Ca-Cu-O Family

BSCCO members share the common chemical formula $Bi_2Sr_2Ca_{n-1}Cu_nO_{2n+4+\delta}$ in which n denotes the number of cooper atoms and the number of copper-oxide planes in a unit cell in the same time. The calcium atoms separate the copper-oxide planes where superconductivity happens. Besides the metal elements, the oxygen content can also affect superconductivity of BSCCO crystals including T_C [18, 19], anisotropic normal-state resistivities [1, 2], and vortex pinning [20]. Similar with other oxide superconductors, BSCCO is sensitive to oxygen composition. These BSCCO compounds can have different T_C values with varied amount of oxygen in the materials. The doping level of oxygen is defined to be optimal doping when their highest T_C is achieved. Any doping level above (overdoped) or below (underdoped) the optimal doping can lead to lower T_C. Precise control of doping is quite challenging but necessary during the synthesis process by controlling the annealing temperatures and oxygen pressure. A series of studies of oxygen doping level has been done

to control the crystal properties [21, 22, 23, 24] The change in stoichiometric structures can significantly affect the phases of BSCCO crystals with different properties [25, 26].

$Bi_2Sr_2CaCu_2O_{8+\delta}$ (Bi-2212) [27, 28] with two copper-oxide layers in the unit cell and $Bi_2Sr_2Ca_2Cu_3O_{10+\delta}$ (Bi-2223) [29] with three copper-oxide layers were reported to have T_C of 80 $\sim$ 110 K higher than 30 K in Bi-2201 case which only has a single copper-oxide layer in its unit cell. Their crystal structures and lattice constants were also identified. These members share similar values on the a-b plane with $a \approx 5.4$ Å and $b \approx 5.4$ Å. The differences between them is the height of a unit cell along the c-axis. More copper-oxide planes in the unit cell indicate a taller crystal structure. Bi-2201 has $c \approx 24.6$ Å; Bi-2212 has $c \approx 30.7$ Å; Bi-2223 has $c \approx 37$ Å. Some groups also tried to synthesize BSCCO crystals with more copper-oxide planes such as the phases of Bi-2234 and Bi-2245 [30, 31, 32]. However, with more copper-oxide planes, the crystal structures also grow taller with $c \approx 42$ Å for Bi-2234 and $c \approx 50$ Å for Bi-2245. Therefore, these phases are less stable and more sensitive with the substrate temperatures during synthesis which makes them more difficult to grow. Their T_C values start to drop and become lower comparing with Bi-2223 phase which has the highest T_C among BSCCO members so far.

5.1.3 Two-Dimensional HTS with Anisotropic Properties

The crystal structures of BSCCO were revealed by high-resolution transmission electron microscopy and x-ray diffraction patterns [17]. Tarascon's group further calculated the distances of bonds in the structure of Bi-2212 [25]. They found one of the bismuth-oxide bonds has the longest distance about 3.0 Åamong all other bonds. This implies that the

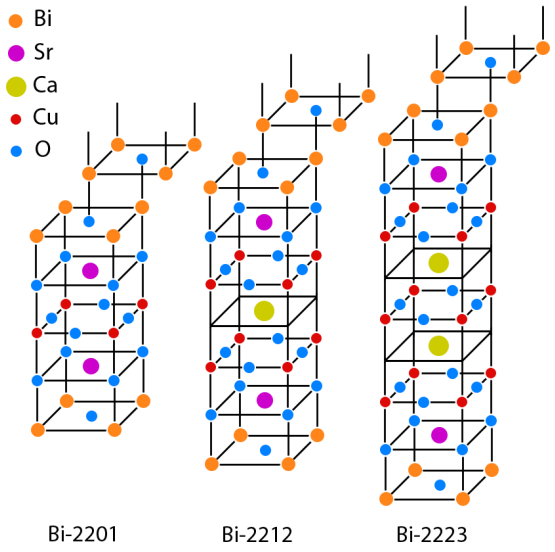

Figure 5.2: The unit cells of Bi-2201, Bi-2212, and Bi-2223

bismuth-oxide layers are only weakly bonded with each other. Later in the reports using scanning tunneling microscopy, they further confirmed the cleaved surfaces were bismuth-oxide layers by comparing the periodicity of corrugation [33, 34]. BSCCO was confirmed as a two-dimensional layered cuprate HTS with the cleaved planes at bismuth-oxide layers where are weakly bonded by the van der Waals forces. The BSCCO single crystals employed in this dissertation is Bi-2212, and the following discussions will mainly focus on the studies of Bi-2212 properties.

Bi-2212 single crystals have the perovskite structure (ABO_3 composition) [35] with the lattice constants of $a = 5.4$ Å, $b = 5.4$ Å, and $c = 30.7$ Å. Such a tall structure of Bi-2212 leads to the extremely anisotropic transport properties in both of its normal and superconducting states. The normal-state resistivities of Bi-2212 single crystals were

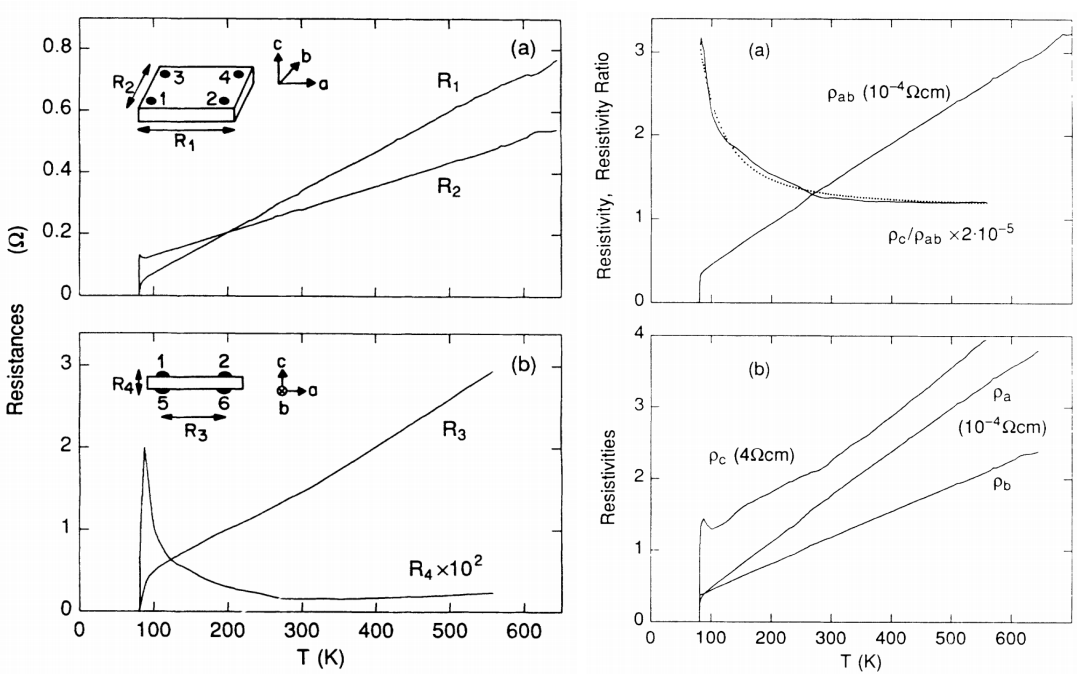

Figure 5.3: The anisotropic resistivity along different directions of single-crystalline Bi-2212 [1, 2]

found different along different orientations [1] and the results were reproduced again [2]. Significant anisotropy has been found between in-plane (a-b plane) and out-of-plane (c-axis) orientations. The resistivity along c-axis (ρ_c) was measured about four to five orders of magnitude larger than the resistivities along the a (ρ_a) and b-axis (ρ_b). On the a-b plane, ρ_b is less than ρ_a, and this indicates the highest conductivity is along with the direction of superlattice of Bi-2212.

Aside from in the normal state, Bi-2212 single crystals also exhibit high anisotropy in the superconducting state. Penetration depths at 0 Kelvin vary a lot between the in-plane ($\lambda_{a-b}(0)$) and out-of-plane ($\lambda_c(0)$) directions based on the results of microwave experiments [36, 37] and the critical field measurements [38, 39, 40, 41]. The average value of $\lambda_{a-b}(0)$

from previous reports ranges from 200 nm to 300 nm, whereas $\lambda_c(0)$ is up to micrometer level (40 μm in ref. [36] and 100 μm in ref. [38]). The huge difference between $\lambda_{a-b}(0)$ and $\lambda_c(0)$ in the superconducting state can be correlated with the results between ρ_{a-b} and ρ_c in the normal state. The big value of $\lambda_c(0)$ leads to a speculation of weak coupling superconductivity between the layered copper-oxide superconducting planes in the structure.

Coherence lengths at 0 Kelvin were extracted with the similar experiments for penetration depths. From the critical field measurements, the coherence lengths were determined around 2 $\sim$ 4 nm on the a-b plane ($\xi_{a-b}(0)$) and only a few angstroms (Å) along the c-axis ($\xi_c(0)$) [42, 43, 44, 45]. The values are quite close to the results in other experimental methods of conductivity [46] and point-contact tunneling [47] and theoretical calculations [48]. Similar with other cuprate superconductors, Bi-2212 has extremely short coherence lengths along any directions, and some concluded this is a consequence of low current density in cuprate HTS [46].

The small value of in-plane $\xi_{a-b}(0)$ is the main challenge for fabricating the planar Josephson devices on the a-b plane of Bi-2212. The barriers of the devices need to be very thin to maintain carriers couplings, and with high potential to observe cooper pairs tunneling without too much quasi-particles tunneling. Thus, to fabricate an a-b plane Josephson junction with Bi-2212, the barrier needs to be narrow and insulating. The thickness of a double cooper-oxide layer separated by a calcium atom (Cu-O/Ca/Cu-O) in a unit cell of Bi-2212 is around 4 Åwhich is comparable with the average $\xi_c(0)$ value of 1 $\sim$ 4 Å. This supports the statement that superconductivity comes from the copper-oxide

planes.The coupling along Bi-2212 c-axis is very weak based on the short $\xi_c(0)$. This value is even smaller than the spacing between the double copper-oxide layers separated by the bismuth-oxide layers ((Cu-O)$_2$/Bi-O/(Cu-O)$_2$) in Bi-2212 crystal structure, which is about $s = 12 \sim 15$ Å. The condition of $\xi_c = s$ becomes the critical crossover for determining the dimensions of the materials. When ξ_c is larger than s ($\xi_c > s$), the three-dimensional (3D) Ginzbur-Landau mean-field theory is applicable to to describe the superconducting order parameters. However, the two-dimensional (2D) Lawrence-Doniach model [49] modifying from the Aslamazov-Larkin equation [50] will be more realistic to depict the behaviors when ξ_c is less than s ($\xi_c < s$).

5.1.4 Intrinsic Josephson Effect

From previous discussions, there are bismuth-oxide layers and double copper-oxide superconducting planes in a unit cell of Bi-2212. The bismuth-oxide layers are weakly bonded with van der Waals forces so that Bi-2212 can be easily cleaved like other two-dimensional materials such as graphite. From the crystal structure of Bi-2212, the distance between two double copper-oxide planes is revealed to be around 12 Å, which is way longer than its estimated ξ_c around 1 to 4 Å based on any current theoretical models. All of these factors contribute to the fact that transport along c-axis is less preferable then the directions in-plane with the copper-oxide planes on the a-b plane. Such highly anisotropic characteristics make Bi-2212 a two-dimensional cuprate HTS, and even lead to formation of the intrinsic Josephson effect.

In 1991, existence of intrinsic Josephson effects has been found between the stacks of Bi-2212 crystal structure by Kleiner's group [51]. The intrinsic junctions are oriented

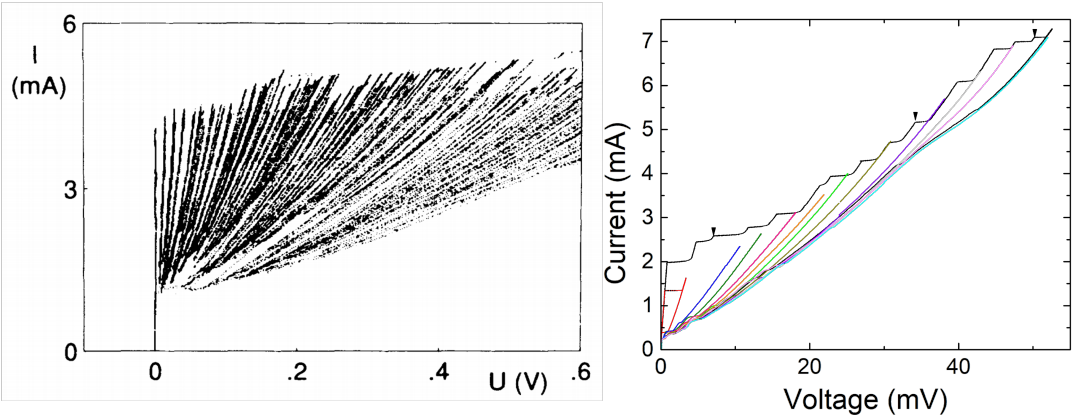

Figure 5.4: Intrinsic Josephson junctions measured by Kleiner *et al.* (left) and us (right).

along the c-axis of the crystals. The weakly bonded bismuth-oxide planes serve as the insulating barriers of the intrinsic junctions, and the double copper-oxide planes act as the separated superconducting electrodes.

They observed several branches in the current-voltage (I-V) relations of a small Bi-2212 single crystal. The discrepancy between two consecutive branches in the normal-state region is equally distributed. The reason of this phenomenon is thus concluded to be that the number of involved intrinsic junctions in the resistive voltage range is increasing when applying higher energy. In other words, each step of the branches implies adding one more additional in-series intrinsic junction of the Bi-2212 stacks. The uniform distribution also rules out the potential exotic junctions caused by cracks in the crystals. As shown in Fig. 5.4, we also obtained similar results from our Bi-2212 crystals with less branches because the thickness of our exfoliated thin-film-like crystals were less than 100 nm in contrast to the thicker crystals they used in the work. The number of branches in I-V

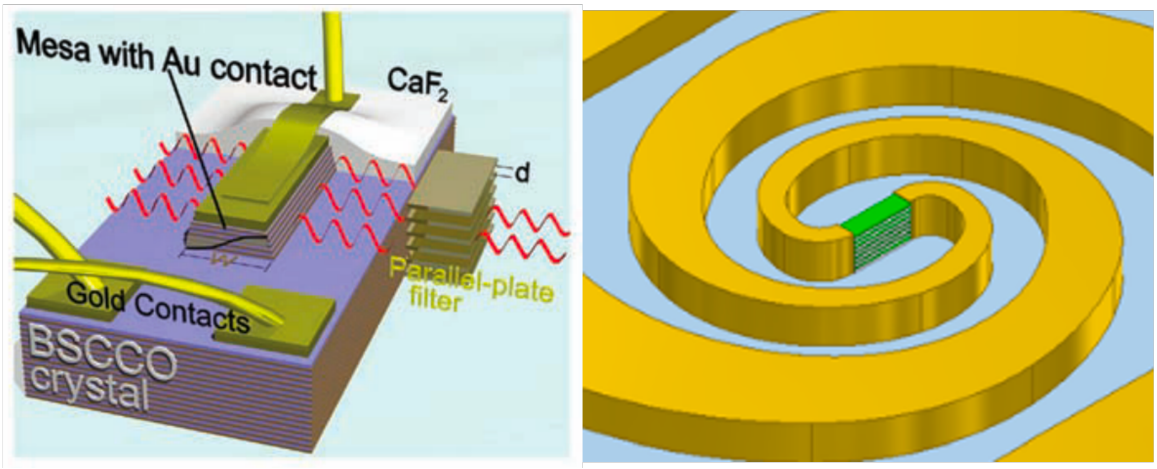

Figure 5.5: Mesa-like devices to expose the intrinsic junction stacks for microwave emission and detection.

also correlates with thickness of crystals since a single intrinsic junction has a stack height around 15 Å(half of a unit cell height 30 Å). They also did AC measurements and microwave experiments to verify mutual phase locking and self-synchronization of intrinsic junctions. The number of locked intrinsic junctions was reported to be around the order of ten and up to 200 intrinsic junctions are involved in the microwave emission and form the Shapiro steps. The strong responses and synchronizations can be the indications that these intrinsic Josephson junctions share uniform junction properties and only have small deviations in the characteristics.

The same group further confirmed the type of intrinsic junctions to be SIS with the layers of bismuth-oxide and strontium-oxide as the insulating barriers instead of weak links [52]. From the microwave experiments, they found all 2000 intrinsic junctions in a 3-μm thick crystal contributed to the radio-frequency (rf) emission. This again proves the uniformity of intrinsic junctions and makes Bi-2212 crystals an excellent radiation source

or sensors of high-frequency signals for communications [53, 54, 55, 56]. Bi-2212 crystals are often fabricated into mesa-like structures (as shown in Fig. 5.5) to expose the intrinsic junctions for detecting their *rf* radiation. With the intrinsic *c*-axis Josephson junctions, Bi2212 can be a potential platform to realize the multidimensional superconducting circuits if any fabricated junctions can be created on the *a*-*b* plane.

5.1.5 Ion Disordered $Bi_2Sr_2CaCu_2O_{8+\delta}$

In previous studies, a new technique of a focused helium ion beam (He-FIB) has been implemented to fabricate Josephson junctions on the *a*-*b* plane of YBCO thin films [5], and furthermore these He-FIB junctions were applied in SQUIDs [57, 58]. This technique utilizes the effect of ion irradiation that causes significant impact on superconductivity of cuprate HTS. Similarly, superconductivity of BSCCO, also a cuprate HTS, can also be affected by ion disorder with reduction of the critical temperatures T_C and widening of the transition widths [59, 60]. They become insulating after ion implantation with sufficiently high doses of neon and helium ions.

In the report of Matsui *et al.* [59], they used 200-keV neon ions to implant the bulk crystals of Bi-2212 and observed noticeable damage on the irradiated crystal. Above a certain ion dose, the transition was vanished and the resistance grew extremely high at lower temperatures. They also provided comparisons between the resultant T_C of Bi-2212 and YBCO irradiated with different ion doses. The required dose for BSCCO transitioning to an insulator from a superconductor is lower than YBCO with the same thickness, which implies BSCCO can be more sensitive to ion disorder than YBCO.

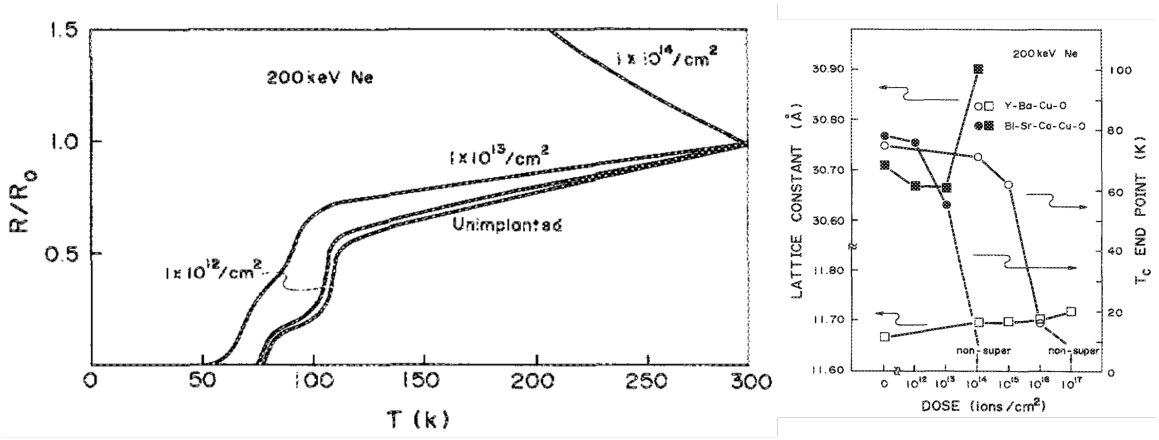

Figure 5.6: The effects of neon ions onto Bi-2212.

Later Aruga *et al.* [60] did the similar experiments with 400-keV helium ions to Bi-2212 films and acquired the same tendency of more suppressed superconductivity by ion implantation with increasing ion doses. They tried to process the samples with post-annealing to recover damaged superconductivity after helium ion irradiation. However, beyond the critical ion dose, the superconducting transition never presents again even with post-annealing. Superconductivity of Bi-2212 can be totally destroyed after being irradiated with a helium ion dose greater than the critical dose. Therefore, He-FIB can be a potential technique to irradiate Bi-2212 single crystals and locally disorder the structure for studying *a-b* plane transport properties across the irradiated area. Recently, the author has applied He-FIB to Bi-2212 thin-film-like cleaved single crystals and successfully fabricated a SNS Josephson junction on the *a-b* plan [61]. Chapter 5 will continue the studies of He-FIB junctions on Bi2212 *a-b* planes, and reveal more details of different characteristics of junction fabricated in this way.

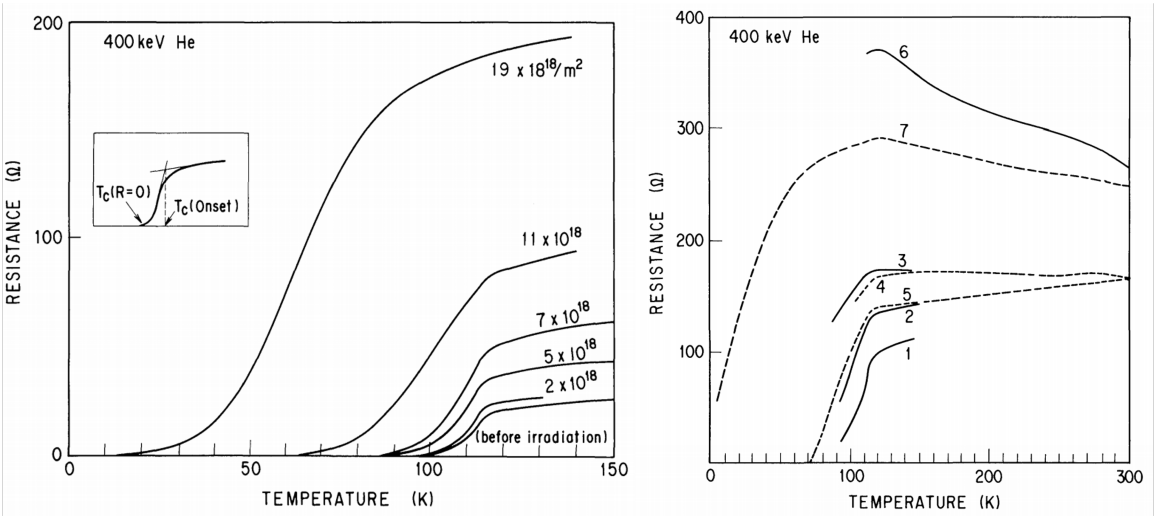

Figure 5.7: The effects of helium ions onto Bi-2212.

5.2 Experimental Methods

This section has been published in early 2021 [61]. Therefore, the details of processing parameters will be reiterated and reordered, but the focus will be shifted to the characteristics of other unpublished junctions. A schematic illustration of a Bi-2212 He-FIB junction is attached below with the defined dimensions for references in the following contexts. The dark and light grey planes indicate the insulating barriers (bismuth-oxide and strontium-oxide layers) and the superconducting copper-oxide planes of the intrinsic junctions in the Bi-2212 crystals. The orange plane perpendicular to the grey planes is the He-FIB junction we proposed to insert.

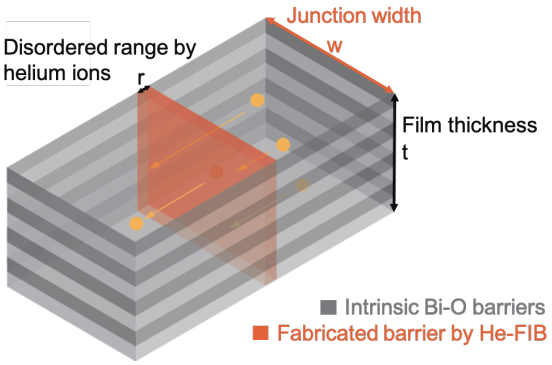

Figure 5.8: The schematic illustrations of He-FIB junctions on a Bi-2212 cleaved crystal with defined dimensions.

5.2.1 Synthesis

The Bi-2212 single crystals presented in this dissertation were synthesized with the traveling solvent floating zone method (TSFZ) by our collaborators from University of Tsukuba [62, 63]. The processing was partially tested with the crystals grown by the other collaborator, Genda Gu from Brookhaven National Laboratory [64]. The oxide powder of each element (bismuth oxides, strontium oxides, and calcium oxides) was mixed with the corresponding stoichiometric ratio. The infrared light was focused by pairs of elliptical mirrors to form the heat source. The mixture of oxide powder was heated with flowing gas of oxygen and argon at specific temperatures and pressures. Studies of BSCCO single crystals synthesis have presented the BSCCO crystal properties with varying oxygen contents by carefully controlling annealing temperatures and oxygen pressure. These single crystals have large sizes with the dimension of one side up to 1 cm.

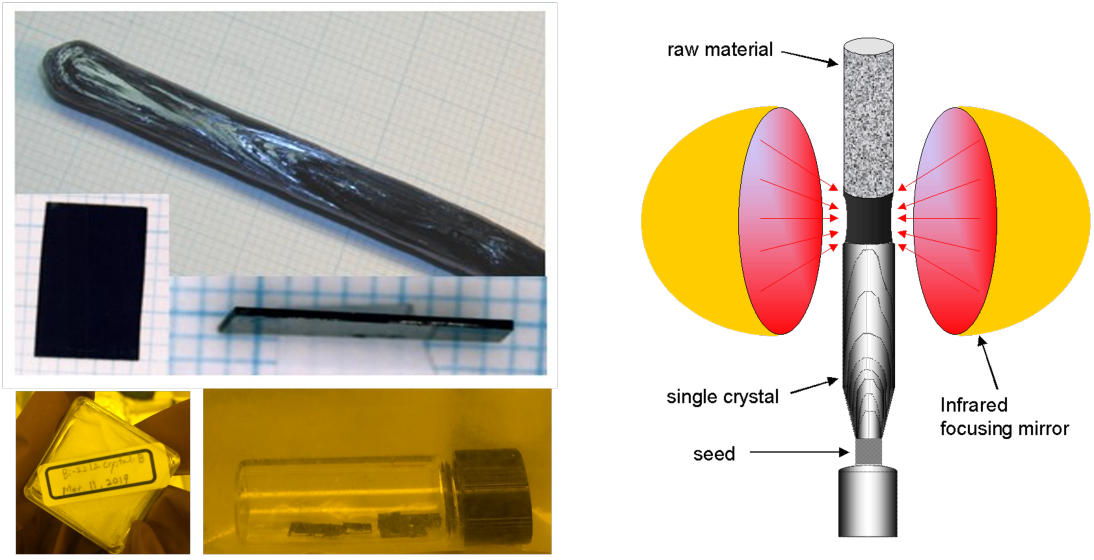

Figure 5.9: Synthesis of bulk Bi-2212 single crystals

5.2.2 Fabrication

Exfoliation

The thin-film-like crystals were mechanically first exfoliated from single-crystalline bulk Bi-2212 using Nitto SPV224 tape (the blue tape), and then stuck the tape without creating any bubbles to the substrates. In prior to removing the tape, the substrates were heated up by a hot plate with surface temperature at 70 $\sim$ 90 °C for 30 sec to assist the attachment between the crystals and substrates. To complete transferring, peel off the tape carefully from the substrates and look for appropriate crystals with a optical microscope. The substrates are 5 mm by 5 mm silicon substrates with 300 nm thick oxidized layer (300 nm SiO_2/Si).The specific substrates were chosen to pick thin cleaved crystals for helium ions to penetrate through. The thickness of Bi-2212 crystals can be roughly estimated by observing the different colors of crystals on the substrates with an optical microscope since

the absorbance ratio of green light varies with thickness [10] (See Table. 5.1).

Color Description	Thickness (nm)
green blue	< 30
light blue	40
yellow green	$60 \sim 70$
burgundy red	80
grey purple	100
bright yellow	120
dark purple	$140 \sim 200$

Table 5.1: Color-Thickness map.

From SRIM simulation results [15] for stopping helium ions distribution, we learned that most of 25-keV helium ions will shoot through an 100-nm thick Bi-2212 layer and stop in the substrate layer. Therefore, a crystal below 100 nm is ideal for the following He-FIB process. Although the penetration depth of helium ions was determined to be around 137 nm, which is greater than the thickness of Bi-2212 layer and means helium ions penetrate through the layer, there is still a wide ion straggle about 100 nm at the bottom of the Bi-2212 layer (r $\sim$ 100 nm at t = 100 nm). The most disordered area is confined within only a few nanometers (r $\approx$ 3$\sim$4 nm) at the surface and is narrower than 20 nm at thickness less than 50 nm (r $\sim$ 20 nm at $t < 50$ nm), whereas the range starts to spread out with lower disorder level at deeper thickness ($t > 50$ nm). In order to have a narrow and strong barrier, thinner crystals ($t < 50$ nm) with larger areas are more ideal candidates for the studies.

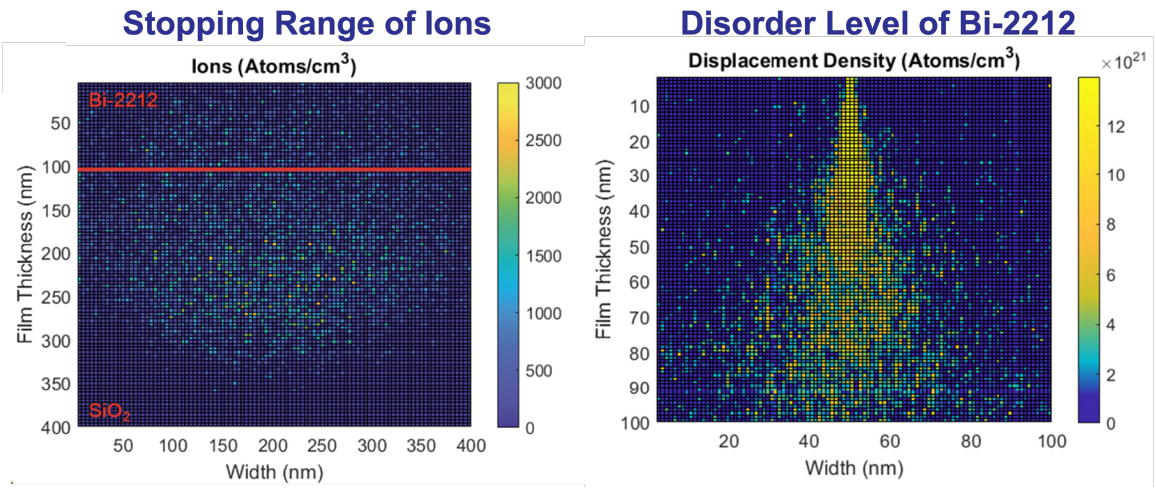

Figure 5.10: SRIM results of a 25-keV into 100-nm thick Bi-2212 and 300-nm thick SiO_2 layer: The distribution of stopping helium ions into both layers (left); A zoom-in view of the disorder level in the 100-nm Bi-2212 layer (right).

Lithography

After transferring the flakes to the substrates from the tape, the substrates along with the cleaved crystals were directly spun with Fujifilm OCG 825 photoresist. Lithography with a g-line laser was thus employed to draw contacts pattern on the sample, and the sample was developed to form the contact pattern on the resist. At least four four contacts are needed to be fashioned on each exfoliated Bi-2212 crystal to do the measurements with the four-terminal configuration. This is especially important to Bi-2212 samples because the leads are made with a normal platinum metal after exfoliation and can cause big contact resistances between the metal layer and the surfaces of Bi-2212 cleaved crystals. In contrast to the case of YBCO, YBCO samples were fabricated with the entire thin films and the metal capping layer was *in situ* evaporated on top of the films, so the electrical contacts were also superconducting because of the YBCO films underneath. The resolution of laser lithography is around 1 μm when patterning YBCO thin films. However, since the lift-off

process is required for Bi-2212 samples, the patterned photoresist of Bi-2212 usually needs to be over-developed. Hence, the safe resolution for Bi-2212 is 2 μm considering the lift-off process. The most stable procedure is established with 4-μm patterned electrodes and at least 4-μm spacing in between because of ultrasonic vibration in the lift-off process.

The number of contacts needs to be more than four, and the minimum width of the contacts is 4-μm and also the smallest spacing of 4-μm. To fit these contacts, the areas of Bi-2212 need to be large with at least one lateral dimension greater than 30-μm so that the electrodes can be evenly distributed on top of the crystals. We also found This is the additional constraint except for thickness when choosing which crystals to process. In conclusion, during lithography process, we tend to choose a larger and thinner cleaved crystal under the optical microscope for a successful lift-off step and helium ion irradiation.

Argon Plasma Cleaning

After conventional lithography process, the samples were cleaned by 50-Watt argon plasma for 30 seconds to 1 minute. Platinum of 80 $\sim$ 100 nm was deposited onto the sample with the AJA sputtering system *in situ* right after the **plasma cleaning**. This cleaning procedure is extremely critical to the whole fabrication for making contacts. The thin-film-like exfoliated Bi-2212 crystals, which are only a few nanometers thick, are more sensitive to the surrounding than the whole bulk Bi-2212 single crystals [65]. Hotta*et al.* studied the effects of organic solvents to BSCCO crystals by soaking them into various solvents and water for long time. They found exposure to water and these solvents can be harmful for superconductivity of bulk crystals by reduction of T_C. This is more severe for the thin cleaved crystals.

Therefore, once the crystals are cleaved, it is better to finish contacts fabrication as soon as possible to avoid photoresist sitting on the crystals and air exposure for too long. While the use of solvents is inevitable, the fabrication procedure mentioned in this section still reduces much exposure to other chemicals comparing to the general fabrication processing which involves multiple times of lithography and milling.

In the beginning, we tried to deposit gold as the contact metal with e-beam evaporation. However, the evaporator doesn't have a plasma system inside the chamber, so the cleaning process cannot be done *in situ* which leads to extra surface exposure to the air. In addition, gold doesn't stick very well with Bi-2212 crystals with very few diffusion into Bi-2212, which may due to large differences between the chemical potential of gold and Bi-2212 at the contact surfaces. The electrical leads are easier to be broken after lift-off with evaporated gold. The contact resistances of Bi-2212 samples fabricated with this method were very large with values up to megaohms, which hindered observation of I-V relations through clean measurements. We speculated the cause of huge contact resistances is the potential dead layers on the surface after long exposure to the environment during processing. To improve the attachment of leads to Bi-2212 surfaces, a surface treatment is required, and another alternative for metallic contacts is needed to replace gold.

Sputtering

Based on previous experiences, I adjusted the procedure and switched to the AJA sputter system with *in-situ* argon plasma and a heater for heating up substrates. The contact metal was selected as platinum, which has exhibited better stick ability to the sample surfaces. The detailed procedure is explained in three parts as follows: sample

loading, sputtering and sample unloading.

Sample loading: After venting the load-lock, the samples were first tapped on to the iron plate as the sample holder and loaded into the arm. The plate has the carving markers at its side, and it needs to be placed with markers facing the window for later steps. Start to pump down the load-lock parking space until its pressure goes below 5×10^{-6} torr to open up the valve between the sample parking arm and the main chamber to avoid contamination. Remember to raise the central grabbing stick to the highest position before extending the arm into the main chamber in order to prevent crushes. Push the arm into the sputtering chamber and the sample plate should locate right underneath the stick. The central stick for grabbing the sample plate has three claws. Lower down the central stick slowly to approach the arm and align one of its claws to the plate markers. Insert the central stick into the plate and turn clockwise to grab the plate. Check if rotation of the stick along with the iron plate is smooth or not. If not, the iron plate needs to be dropped back down to the arm and redo the alignment. If the plate rotates uniformly, retract the load-lock arm and close the valve.

Sputtering: Turn on the DC power supply and set the main chamber to the pressure mode. This will close halfway of the valve between the chamber and its pump to control the argon pressure later. Drop down the rotating plate to be close to the plasma source at the bottom of the sputtering chamber, flow argon gas ($\sim$ 10 sccm) and ramp up the power supply to around 50 Watt (6 %) to fire up the plasma. See the button of plasma turn pink. Time 30 second to 1 minute for the argon plasma cleaning. Set the substrate heater to 70 °C at the first, and once it reaches 70, increase the temperature to 90 °C slowly

to prevent overheating. Bring up the plate to the height at the value of 40 and ramp down the power to the corresponded output (20 Watt at 2.5 %) for platinum sputtering. Close the window port shutter to avoid extra coating to the glass. Open the target shutter of platinum and start timing for 35 to 40 minutes. Shut off the heater when the target shutter has been opened for 5 minutes. Once sputtering is finished, close the target shutter and ramp down the power supply to zero.

Sample Unloading: Turn off the power supply and stop flowing argon. Set the main chamber to the "Open" position to pump out extra argon gas. Stop rotation and raise the central stick along with the sample plate to the highest position. Open the valve between the main chamber and the load-lock and insert the arm into the chamber. Bring down the plate to the arm and turn the stick counterclockwise to loosen the plate. Retract the arm and shut off the valve. Vent the parking space and take out the iron plate. Be cautious when touching the plate because the surface may still be hot after the heat treatment.

Lift-Off

The final step for making the electrical contacts is the lift-off process. The whole surfaces of samples were covered with platinum with a layer of patterned photoresist underneath. The samples were thrown into a small beaker filled with acetone. The photoresist is washed away by acetone in ultrasonic bath around 35 to 45 °C for 10 seconds at first, and increase 5 seconds each time to avoid broken leads if there is platinum residual between the contacts. Flush the samples with isopropanol and dry them with nitrogen gas to reduce possible solvents residue on their surfaces. The thin-film-like cleaved single crystals of Bi-

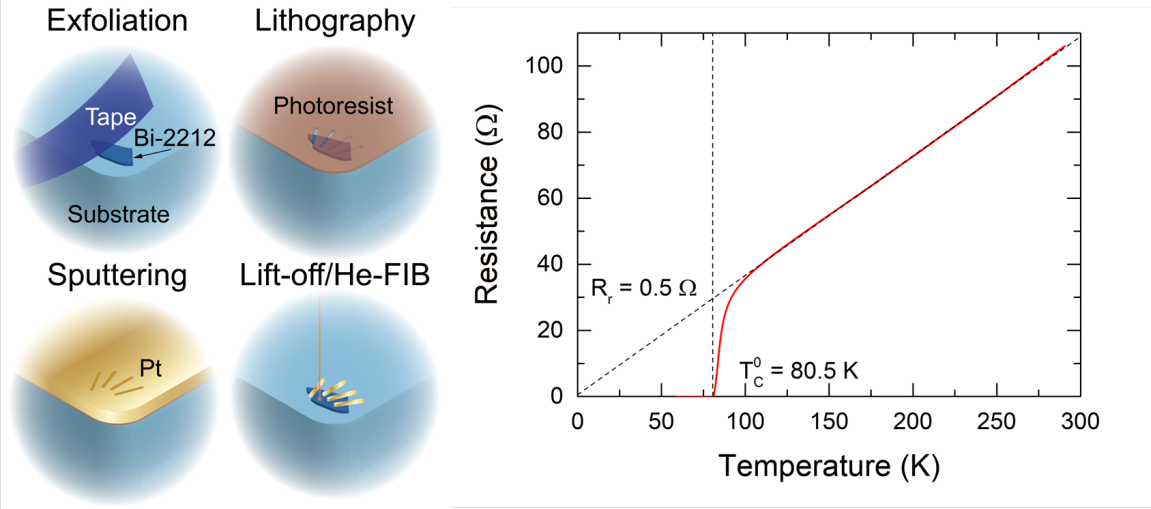

Figure 5.11: Left: A schematic illustration for fabrication procedure. Right: R-T result of a Bi-2212 crystal after contacts preparation with the lift-off process.

2212 has been prepared with the platinum electrical contacts. The schematic illustration of the complete procedure for contacts fabrication is presented in Fig. 5.11.

Resistance-Temperature Measurement

To examine superconductivity of Bi-2212 crystals, a measurement of resistance versus temperature (R-T) is done after preparation of the contacts. The superconducting transition at around 82 K is observed from the result of Fig. 5.11. Low residual resistance shows that the Bi-2212 crystal after processing still preserves its pristine properties with very few defects in the crystal lattice and therefore low carriers scattering. In summary, the fabrication recipe recorded in this section provides the method to make secured electrical contacts for the next following low-noise measurements without significant harm to superconductivity of Bi-2212 crystals.

Helium Irradiation

Last, to create an a-b plane junction in Bi-2212, the method introduced here is to locally disorder the material by helium ion irradiation by a focused helium ion beam (He-FIB). This step can be separated into two parts as junction writing and size trimming, and an optical image of a Bi-2212 device in the top right panel of Fig. 5.12 shows the configuration of the electrodes and the traces of both steps using He-FIB. The beam is first focused and tuned at the contacts to reduce extra damage on the crystals by irradiation. After the beam is optimized, a full view of the crystal is imaged and a line is drawn across it at the desired position for junction writing as shown in the bottom left panel of Fig. 5.12 and the junction will be located at the position of the red dotted line in the top right panel of Fig. 5.12. The junction width w, as indicated in Fig. 5.8, is thus determined by the lateral dimension of the cleaved crystals which is different for each cleaved crystal. It is unrealistic to find a cleaved crystal with ideal thickness t and width w. To solve this issue, a trimming process is needed to control w.

If the defined w of the cleaved crystal exceeds the Josephson penetration depth, the size of the crystal can be trimmed down with high doses around 10^{17} ions/cm^2 to keep the junction within the short junction limit. To accomplish this, two lines are drawn from two sides of the crystal to the center and overlay on top of the junction line drawn previously as shown in the top right panel of Fig. 5.12 (black solid line: trimming, red dotted line: junction). By doing so, w is redefined to be the size of the small portion in the center which remains as the junction. The bottom right panel of Fig. 5.12 shows a resultant trace irradiated by a helium ion beam with the dose of 6×10^{17} ions/cm^2 at the edge of a Bi-2212

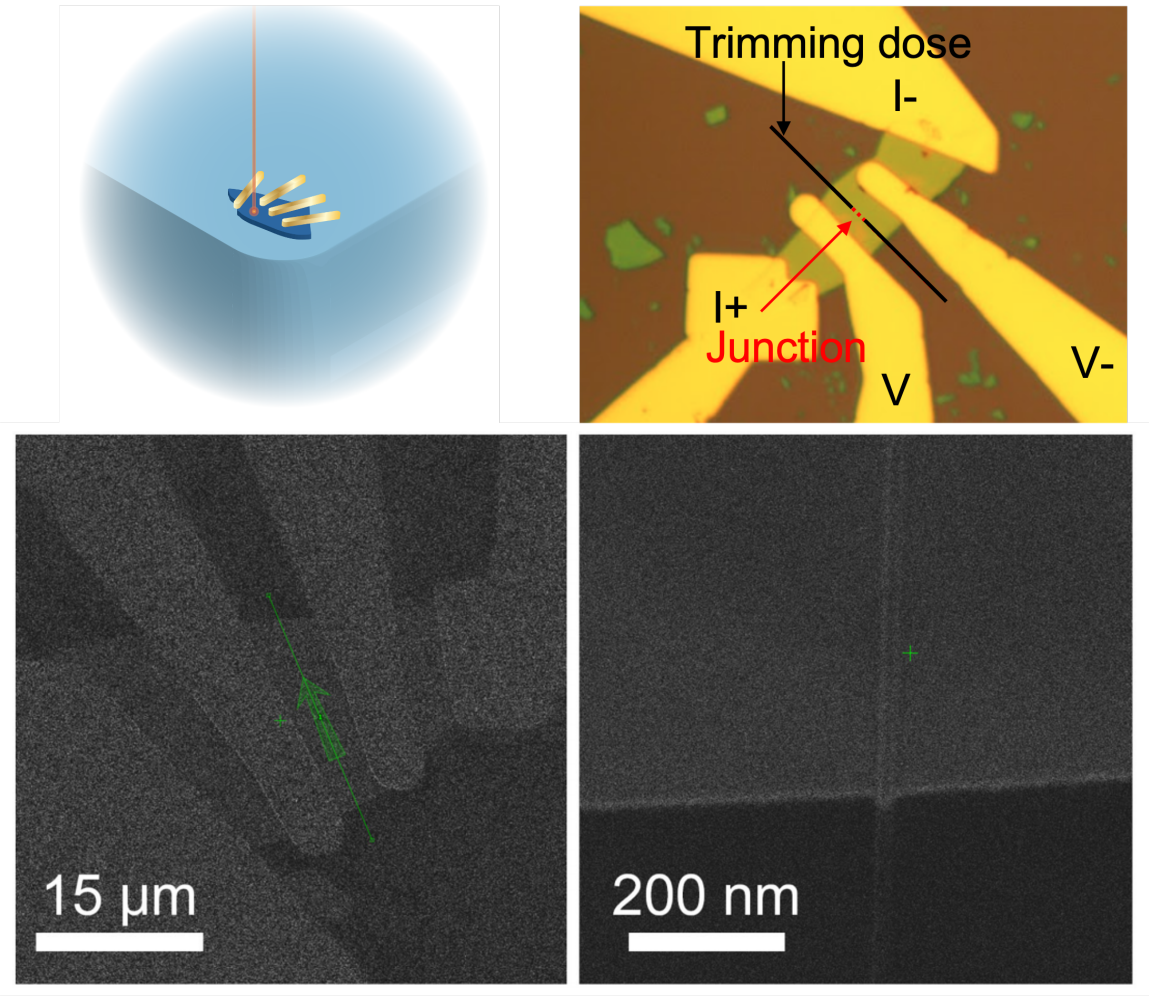

Figure 5.12: Top left: a schematic illustration for a Bi-2212 device irradiated by He-FIB. Top right: an optical picture of a Bi-2212 device and indication for the junction (red dotted line) and trimming traces (black solid lines). Bottom left: the GUI screen view to show the drawn line when writing junction with Zeiss Orion Plus. Bottom right: the resultant trimming trace at the edge of a Bi-2212 crystal cut by a heavey helium ion dose

crystal. The images at the bottom row of Fig. 5.12 are taken with the helium ion microscope (Orion Plus by Zeiss).

Writing junctions is processed before trimming to fabricate uniform junctions. The ion doses for trimming is much larger than the ion doses for writing junctions. If the crystal is trimmed first and the junction is written later, the abrupt change in the ion doses between the two steps, or the sudden switch from the high dose (trimming) to low dose (junction writing), may result in unstable ion doses when fabricating junctions.

5.2.3 Characterization

To ensure the junction was properly narrow down, the topography of the devices was acquired with a commercial atomic force microscope (Horiba/AISt-NT). The round bumps on the background are also observed on the other regions of silicon substrates without the Bi-2212 single crystals on top. Therefore, those bumps are considered as the flakes lifted by the bubbles of substrate after ion irradiation [66]. The traces of helium ion beam with different ion doses are inspected on the surfaces of Bi-2212 flakes with the same thickness 55 nm in Fig. 5.13. The distance between two cuts is about 360 $\sim$ 380 nm, which is slightly smaller than the designed value of 400 nm. Considering the spreading of helium ions, wider damage range may exist below the surface and cause the additional enhancement in resistance. The height of the Bi-2212 crystal is raised by accumulated helium ions after irradiation and compared between different doses. The five repeated cuts with the heavy ion dose of 6×10^{17} ions/cm^2 lifted the flake up to 20 nm and caused the widest damage range. In contrast, the crystal is only raised by 3.5 nm and 2.0 nm separately by the doses

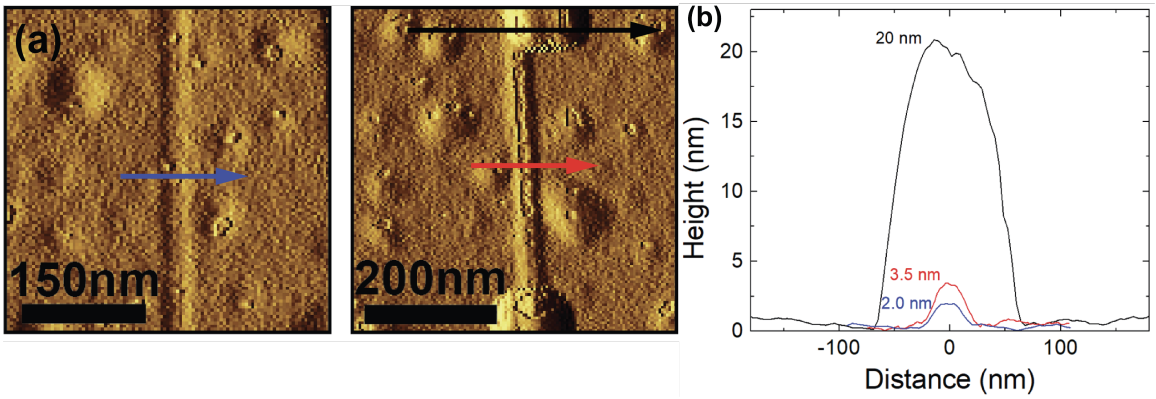

Figure 5.13: (a) Left: Topography of a junction of ion dose 6×10^{16} ions/cm^2 on a 55-nm Bi-2212 cleaved crystal. Right: Topography of the device with a 400-nm wide ($w = 4$) junction of ion dose 7×10^{16} ions/cm^2 on a 55-nm Bi-2212 cleaved crystal. (b) The profile of the 55-nm Bi-2212 crystals with raised height by different ion doses.

of 7×10^{16} ions/cm^2 and 6×10^{16} ions/cm^2.

5.3 Bi-2212 *a-b* plane Junctions by He-FIB

The results of Bi-2212 He-FIB junctions will be discussed in this section. I first studied the junction characteristics with the thin-film-like Bi-2212 fresh cleaved single crystals at $t = 45$, 55, and 80 nm. The junction orientations were confirmed to be on the *a-b* plane by the magnetic field measurements and thus differentiated from the intrinsic junctions of Bi-2212. Similarly with YBCO, I observed the metal-insulator transition in Bi-2212 He-FIB junctions. Furthermore, the junction properties is editable by post-modifications with He-FIB.

5.3.1 *I-V* Characteristics of Bi-2212 at Different Thickness

The different junction behaviors will be presented with the following controlled parameters: junction width ($w = 0.4$, 4, 8, and 10 μm), helium ion doses (3, 4, 6, and

7×10^{16} ions/cm^2), and thickness of the Bi-2212 cleaved crystals (45, 55, and 80 nm). The fabrication parameters of He-FIB is revealed for Bi-2212 single crystals with different thickness for future studies on Bi-2212 crystals with He-FIB.

The other crucial evidence presented here is to confirm the junction orientation through the magnetic field measurements. One of the biggest challenges is to differentiate the fabricated He-FIB junctions on the *a*-*b* planes from the intrinsic junctions of Bi-2212 along the *c*-axis. Based on the geometry of a planar junction, the critical current of the junction should respond to the magnetic field perpendicular to the current flow direction. When applying an external magnetic field applied along the *c*-axis, the *I*-*V* branches of intrinsic junctions are hardly affected with the current flow parallel to the *c*-axis, whereas the He-FIB junctions on the *a*-*b* planes will have a changing amount of Josephson current by sweeping the field.

Cleaved Bi-2212 Crystals with $t = 80$ nm

As references, a set of *I*-*V* was measured before helium ion irradiation. I observed the branch-like structures in the non-linear *I*-*V* at 77 K. The first I_C appeared to be around 1 mA and indicated the critical current of the first intrinsic junction. The inset shows the configuration of voltage and current leads during the measurements.

Ion dose = 3 $\times$ 10^{16} ions/cm^2, $w = 8$ μm: The first sample was made from an exfoliated 80-nm Bi-2212 crystal. The lateral dimension of the crystal is about 100-μm, which is much longer than the Josephson penetration depth for a short junction. The ion dose for writing the junction is 3×10^{16} ions/cm^2 (line dose: 150 ions/nm), and the junction

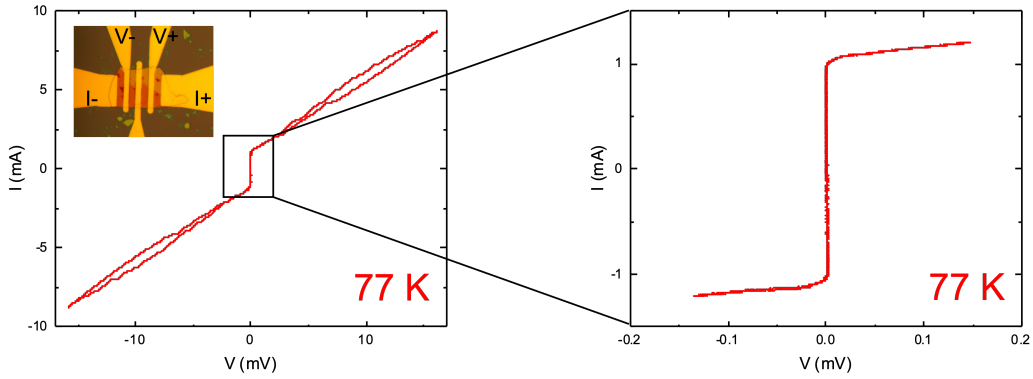

Figure 5.14: Left: I-V relation of an 80-nm Bi-2212 cleaved crystal with no helium ion irradiation (Inset: the optical picture of the sample denoted with the current and voltage leads.) Right: the zoom-in view of I-V at zero voltage and the observed I_C at 1 mA.

width w is defined as 8 μm by the trimming traces of a heavy ion dose of 6 $\times$ 10^{17} ions/cm^2 (line dose: 3000 ions/nm). The first non-zero voltage jump was observed at a suspected I_C of the He-FIB junction of 1 mA at 77 K below T_C of 82 K of Bi-2212. The value of 1 mA is very close the the first branch of Bi-2212 intrinsic junctions, and the suspicious I_C at 1 mA is not responding to the external sweeping magnetic field. More non-linear branches appeared when the sample was cooled down to 10 K. Hence, the 1 mA I_C at 77 K is concluded to be the critical current of the first intrinsic junctions, and no significant changes is found after helium ion irradiation. The ion dose of 3 $\times$ 10^{16} ions/cm^2 may be too low to fabricate a 8-μm Josephson junction on an 80-nm crystal. I first tried to increase the dose and kept w = 8 μm the same.

Ion dose = 6 $\times$ 10^{16} ions/cm^2, w = 8 μm: At the other Bi-2212 crystal, the ion dose for the junction was doubled as 6 $\times$ 10^{16} ions/cm^2 with the same w = 8 μm. The I-V characteristics were measured in a temperature ranging from 8 to 30 K. The I-

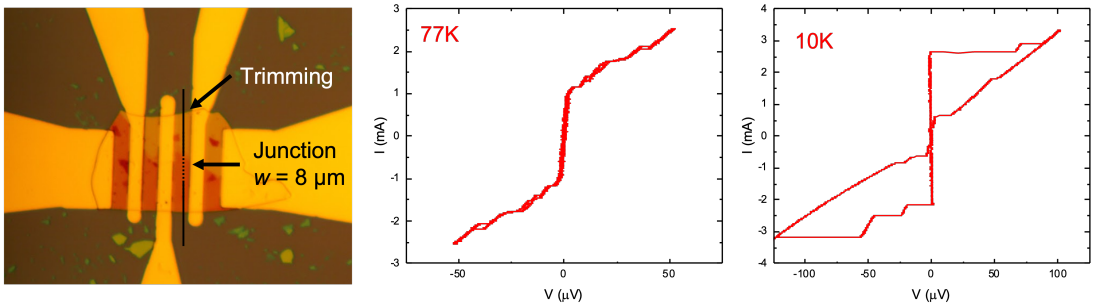

Figure 5.15: Left: the optical image of the 80-nm Bi-2212 device indicated the junction position with 3×10^{16} ions/cm^2 and the trimming traces. *I-V* characteristics of the device measured at 77 K (Middle) and 10 K (Right)

V was obtained in the range of 8 $\sim$ 30 K because the Josephson current vanished above 30 K and became too large and exceeded the limit of achievable measured current values below 8 K. I observed the I_C of this device to be 220 μA at 8 K. Warming up the device is coupled with a decreasing I_C value. In contrast, the normal-state resistance is shown to increase with warming up. The behavior of this device is categorized as a SNS junction with a weak-linked barrier. To extract the junction parameters, each *I-V* curve was fitted with the resistively shunted junction (RSJ) model. As shown in Fig. 5.16 (a), I_C increased rapidly as cooling down due to the increased excess current from quasi-particles tunneling. Additionally, the resistance decreased as the temperature decreased, and showed a normal-metal-like behavior with less scattering at low temperatures. These characteristics are typical SNS junction behaviors. Therefore, this device is categorized as a SNS junction with a metallic or weaker superconducting barrier. Furthermore, a magnetic field along the *c*-axis of the film was applied with an external coil of the dip probe and a nearly perfect Fraunhofer pattern in changing I_C was observed. The period of the pattern is estimated to be between 32 $\sim$ 45 μT, which corresponds to a junction size of 9 $\sim$ 11 μm using Rosenthal's

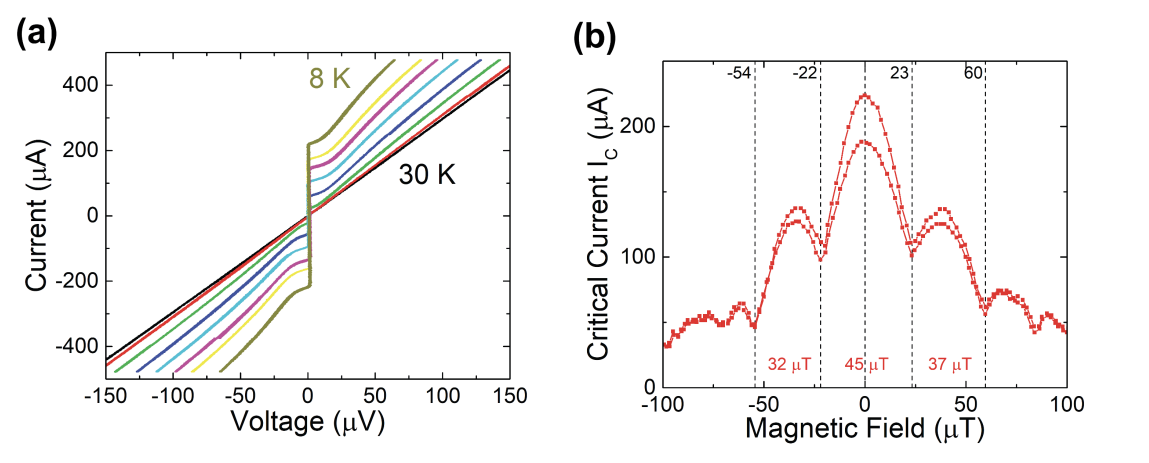

Figure 5.16: (a) The *I-V* relations measured from 8 to 30 K. (b)The nearly perfect Fraunhofer pattern formed by the changing I_C of the Bi-2212 device in (a) by modulating an external magnetic field perpendicular to the crystal.

equation [9]. This estimation is close to the intended value set during the irradiation with He-FIB. The other noticeable point is the local minimum of I_C didn't fall to zero exactly, for example, at the magnetic field $\mathbf{B} \approx 25\ \mu$T, 50 μT, and the side bands. This is because only the supercurrent from Josephson tunneling will respond to the magnetic field while the excess current from quasi-particles tunneling through a weak barrier will not. The remaining current at the side band is around 50 μA, which implies there is excess current around 50 μA in the total I_C value of 220 μA.

Cleaved Bi-2212 Crystals with $t = 55$ nm

The lateral dimension of the 55-nm thick Bi-2212 cleaved crystal was measured to be around 12 μm, which is comparable to the short junction limit, so the first attempted junction was irradiated by the ion dose of 6×10^{16} ions/cm^2 without additional trimming process on this crystal as shown in the left image of Fig. 5.17. The ion dose of

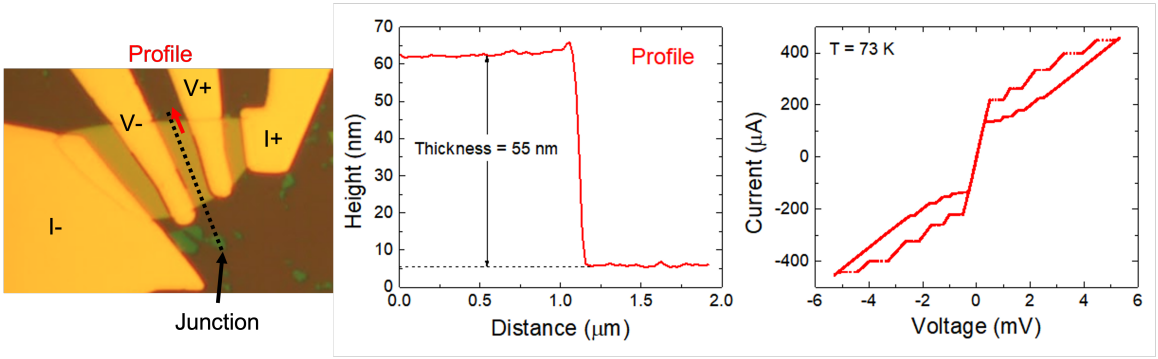

Figure 5.17: Left: the optical image of the 55-nm Bi-2212 device indicated the junction position with 3×10^{16} ions/cm^2 without the trimming traces. Middle: the profile of the 55-nm cleaved crystal along the red arrow shown in the left image. Right: I-V characteristics of the device measured at 73 K.

6×10^{16} ions/cm^2 resulted again in a SNS type Josephson junction with $w = 12$ μm defined by the lateral dimension of the cleaved crystal. The behavior of the junction with $w = 12$ μm and $t = 55$ nm (the left graph of the top row in Fig. 5.18) was fabricated by the same dose of 6×10^{16} ions/cm^2 with the junction with $w = 8$ μm and $t = 80$ nm in Fig. 5.16. Their I-V characteristics appeared to be similar in the values of I_C around 200 μA and R_N less than 1 Ω. Notice the junction ($w = 12$ μm; $t = 55$ nm) has $I_C \approx 220$ μA at 4.2 K, and the other junction ($w = 8$ μm; $t = 80$ nm) has $I_C \approx 200$ μA at higher temperatures around 8 K. From the similar characteristics, the same ion dose may cause equivalent disorder level in the 55-nm crystal with wider width of 12 μm ($0.055 \times 12 = 0.66$ μm^2) and 80-nm cleaved crystals with a narrower width of 8 μm ($0.08 \times 8 = 0.64$ μm^2), because they have similar areas for the current to flow through.

Another junction was also made on a 55-nm thick exfoliated crystal with a slightly heavier ion dose of 7×10^{16} ions/cm^2 (line dose: 350 ions/nm) and a narrower defined w as 4 μm by trimming. There is a significant reduction in the value of I_C from 220 to

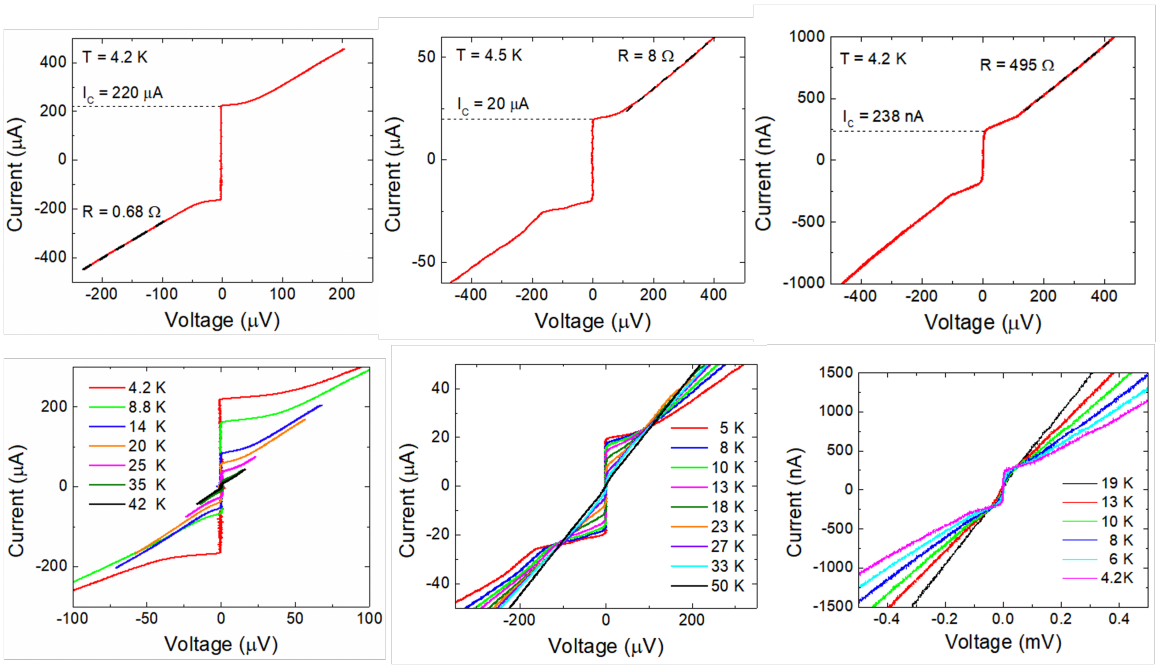

Figure 5.18: Temperature dependent I-V characteristics of the Bi-2212 device with $t = 55$ nm and $w = 12$ μm by the helium ion dose of 6×10^{16} ions/cm^2 (left column), $w = 4$ μm by the helium ion dose of 7×10^{16} ions/cm^2 (middle column), and $w = 0.4$ μm by the helium ion dose of 6×10^{16} ions/cm^2 (right column).

20 μA and an increment in the value of R_N from 0.7 to 8 Ω at 4.5 K which are presented in the middle graph of the top column in Fig. 5.18. From the temperature dependent *I-V* measurements in the middle graph of the bottom column in Fig. 5.18, R_N is increasing while the sample is cooling down and thus results in a crossing point by multiple *I-V* curves at varying temperatures comparing with the SNS behavior of parallel *I-V* curves in normal-state range with no crossing point. The junction ($w = 4$ μm; $t = 55$ nm) is therefore a SIS junction with a more insulating barrier. For the tunneling experiments introduced in the next chapter, the junction can even be modified to be more resistive by shirking down the junction width from $w = 4$ μm to $w = 0.4$ μm whose results shown in the rightmost column of Fig. 5.18. The modified junction ($w = 0.4$ μm; $t = 55$ nm) has the the parameters of I_C around 238 nA and R_N roughly 500 Ω. The critical current was drastically suppressed and the resistance was increased by almost 62 times. The huge change in both parameters is concluded to be caused by the extra damage underneath the surface of the Bi-2212 crystal.

Cleaved Bi-2212 Crystals with $t = 45$ nm

Another Bi-2212 cleaved crystal has thinner thickness of 45 nm and narrower dimensions of 10 μm. A lighter ion dose of 4×10^{16} ions/cm^2 (ion dose: 200 ions/nm) was used without trimming to avoid damaging the material, and therefore w was defined as 10 μm. The *I-V* characteristics is shown in Fig. 5.20 with large I_C of 200 μA at 8 K and R_N of 15 Ω. When biasing the input current at a fixed voltage, the voltage modulated to the sweeping external magnetic field, and the response therefore confirmed the existence of Josephson junction.

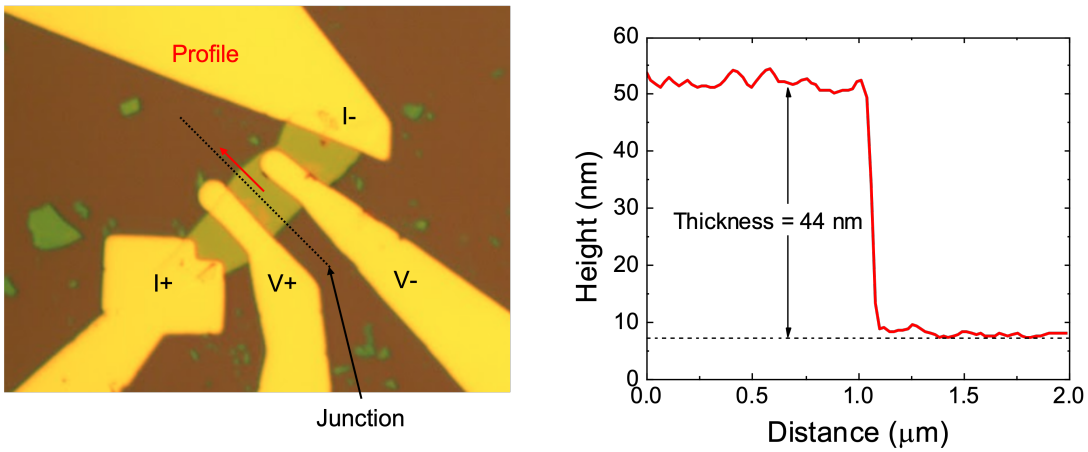

Figure 5.19: Left: the optical image of the 45-nm thick Bi-2212 crystal Right: the profile along the red arrow in the left picture.

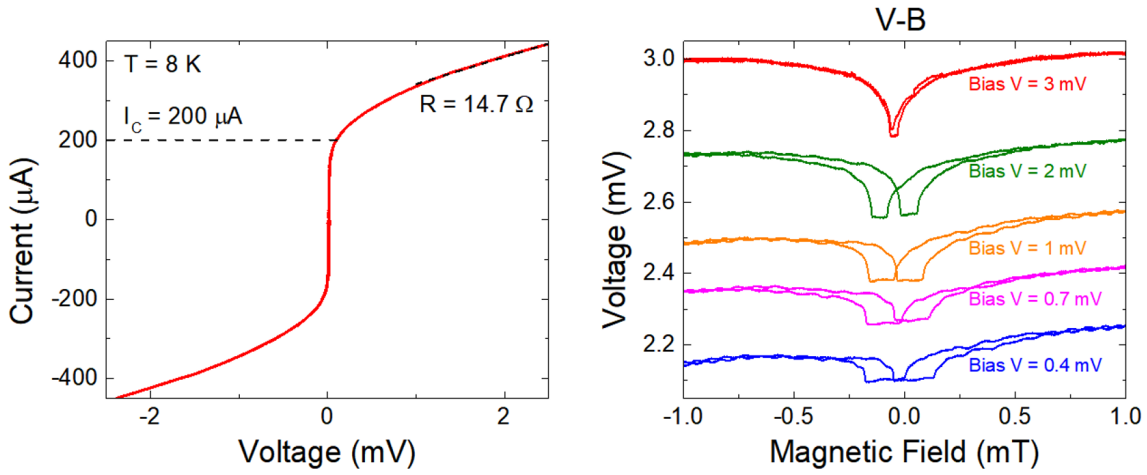

Figure 5.20: Left: I-V characteristics of the Bi-2212 device with $t = 45$ nm and $w = 10$ μm measured at 8 K. Right: the voltage response of the device with the magnetic field (V-B).

A post processing was performed on this device that addition junction was inserted on the same crystal. The light dose leaded to a SNS-like junction and another junction with heavier dose and narrower width was fabricated on the spare area of the cleaved crystal. The new inserted crystal was irradiated by the ion dose of 6.5×10^{16} ions/cm^2 (line dose: 325 ions/nm) with a defined w as 4 μm by the trimming process. The two junctions coexisted on the same cleaved crystal and the new *I-V* measurements after re-irradiation provided the evidence of two in-series junctions. At 4.2 K, I_C was measured as 22 μA, which was a very different value from the previous 200 μA at 8 K, and thus it is the critical current from the new inserted junction with $w = 4$ μm made in post processing. The new R_N was measured to be 8.8 Ω instead of the original value of 15 Ω or an add-up value of two resistances. The reason may be due to extraction of 15 Ω from a small segment not too far into the normal-state voltage regime. In the temperature dependent *I-V* measurements, the behavior were clearly dominated by the new SIS-like junction with $w = 4$ μm at temperatures below 20 K, while the original SNS-like junction ($w = 10$ μm) started be more involved while warming up above 20 K.

To examine the junction with $w = 4$ μm, the magnetic field was applied again to observe the changes of I_C. To exclude the behaviors of the previous SNS-like junction, the sweeping range of current source was maintained below its I_C to focus on the changes of new inserted junction with $w = 4$ μm. Again the modulating I_C formed a nearly perfect Fraunhofer pattern with the local minimum falling close to zero. This implied the value of I_C is mostly consisted by the supercurrent from Josephson cooper pairs tunneling and very few by the excess current from the quasi-particles tunneling, and therefore the new inserted

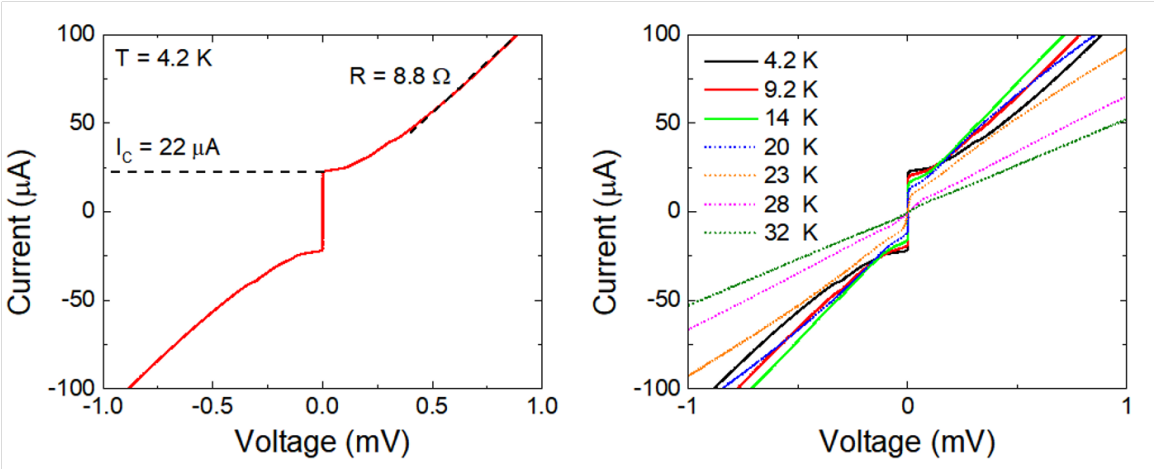

Figure 5.21: Left: I-V characteristics of the new inserted junction with $w = 4$ μm at 4.2 K. Right: the temperature dependent I-V measurements of two junctions in-series.

junction with $w = 4$ μm has a strong barrier to screen out tunneling by the electrons (from the broken pairs). The estimated w is $3 \sim 5$ μm with a period of $144 \sim 162$ μT using Rosenthal's method again. The approximation is close to the defined value of $w = 4$ μm by He-FIB, and therefore the Bi-2212 a-b-plane junction fabrication procedure using He-FIB is firmly established with controllable parameters of ion doses and junction widths w based on thickness of cleaved single crystals.

5.3.2 Metal-Insulator Transition

Based on previous investigation for different He-FIB junction parameters, the same phenomenal of metal-insulator transition in YBCO thin films is again found in Bi-2212 single crystals. The junction characteristics are controllable by the ion dose and defined width w of He-FIB. The junctions can be designed with He-FIB parameters only considering thickness of the Bi-2212 cleaved crystals. The dimensional size of cleaved crystals is regardless because

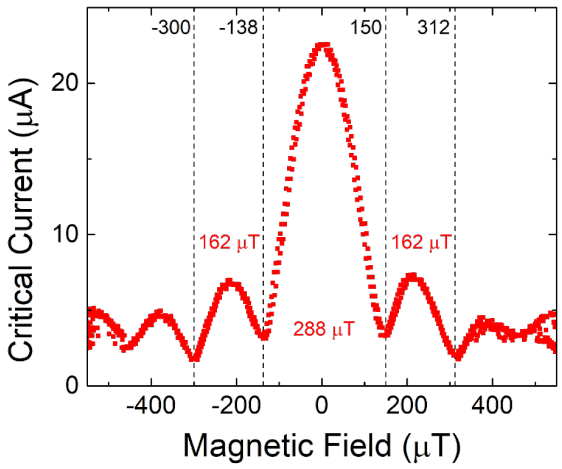

Figure 5.22: A nearly perfect Fraunhofer pattern formed by the responses of I_C to the magnetic field.

the trimming process can confine the current flowing area and thus define the junction width w. The barrier can be tuned as a weak superconductor, normal metal, or insulator by increasing the helium ion doses according to the crystal thickness. A complete detailed table including thickness (t), junction width (w), and the ion dose will be helpful for future processing and further studies. The superconducting circuit can be advanced with the controllable He-FIB junctions and further developed into a three-dimensional design with incorporating c-axis intrinsic Josephson junctions of Bi-2212.

5.3.3 Post Modification

Another advantage of He-FIB junctions presented here is the flexibility to design and re-modify the junction position and behaviors. One can avoid surface defects or dusts easily by placing junctions at another chosen regions at any angles. For circuit development, this process provides the convenience of direct-written junctions like a printed circuit board.

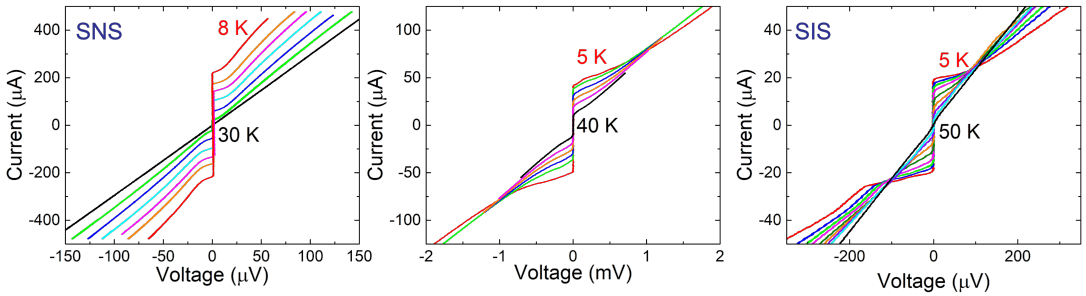

Figure 5.23: Metal-insulator transition of He-FIB Josephson junctions on Bi-2212 single crystals

Furthermore, as I demonstrated in the 45-nm and 55-nm case, the transport properties are adjustable by post processing. This accepts the possibility to improve the circuits when the original barrier is found too weak for performances.

Chapter 6

Tunneling Conductance Studies

Cuprate HTS single crystals with high quality provide a platform to study the superconducting mechanisms behind cuprate HTS because of their uniformity with less disorder in the materials comparing with cuprate thin films. The pairing symmetry of superconducting order parameters remains one of the biggest questions for cuprate superconductors. Several research groups have tried different experimental methods such as microwave measurements to solve the mystery; however there are large variations between their results for the critical values of superconducting parameters such as penetration depths. These studies argued that the differences may come from the disorder and defects in cuprate thin films.

6.1 Introduction

The curtain of new era for advanced computing has been lifted by quantum computation and neuromorphic computation. The essential components of these computa-

tional architectures, such as qubits and artificial synapses, can be built with superconductors. Conventional superconductivity in metallic superconductors has been well predicted by Bardeen-Cooper-Schrieffer (BCS) theory, while the microscopic mechanisms for high-transition-temperature (high-Tc) superconductivity in the complex copper-oxide ceramics (cuprate) remain unclear for years since its discovery. Studying the superconducting (SC) order parameters of cuprate materials can help to understand the functionality of high-Tc SC-based devices and further facilitate the hardware development for the quantum and neuron network.

Direct observation of density of states reveals the characteristic features in the electronic band structures of materials. One noticeable feature is the central peak of supercurrent shown at the zero applied voltage where the Cooper pairs tunneling happens. The bosonic Cooper pairs are formed by the pairing bound states of fermionic single electrons at degenerate energy levels at temperatures lower than Tc. At low temperatures, the supercurrent peak demonstrates the Bose-Einstein condensate of these Cooper pairs. Another important feature is the SC gap in the quasiparticle excitation spectrum at the high-voltage range (100 mV). The size of SC gap (2δ) is the minimum energy required to break the Cooper pairs apart into quasiparticles, that is, the singlet states of electrons. Conventional superconductors exhibit sharper and well-defined edges of SC gap and obey the BCS model, whereas cuprate high-Tc superconductors (HTS) are reported to be gapless in previous works. The V-shape spectra of cuprate are immensely discussed and believed to be a different pairing symmetry from conventional superconductors.

The pairing symmetry of SC order parameters is another puzzle in terms of the

microscopic SC model for cuprate HTS. The BCS theory pictured conventional superconductivity with the spherically symmetric pairing model, s-wave symmetry. The SC characteristics of conventional superconductors are isotropic and uniform along any direction. In contrast, cuprate HTS possess obvious anisotropy in their transport properties of both the normal and SC states. The normal state resistivities of most cuprates are measured to be different along the a, b, and c-axis of their unit cell. For example, a widely studied cuprate HTS,Bi-2212, was found to have much larger resistivity along its c-axis comparing to the a-b plane. It is preferable for carriers to transport along the a-b plane where the SC copper-oxide planes exist in the crystal structure. The SC characteristic 2δ values of cuprate vary a lot along different orientations, and most believe this variation comes from the model of d-wave symmetry with the lobes and nodes. The d-wave model hints the gapless behavior of cuprate HTS can happen at the nodes and the largest gap can be observed along the lobes. Similarly, other SC parameters such as the coherence lengths and penetration depths appear to be highly anisotropic. Careful studies for the electronic band structures of cuprate are beneficial to identify their actual SC mechanisms.

Tunneling conductance measurement is the most common way to provide direct information of the excitation spectrum of quasiparticles and the density of states of materials. The gap-like features in the spectrum are the critical observable to compare with the fundamental SC order parameter 2δ. These measurements require a well-established barrier to obtain clean spectra from the pristine materials. This is difficult especially for cuprate materials because they are sensitive to the environment and the surfaces are easily degraded due to deficiency of oxygen content in the crystal structures. Potential degra-

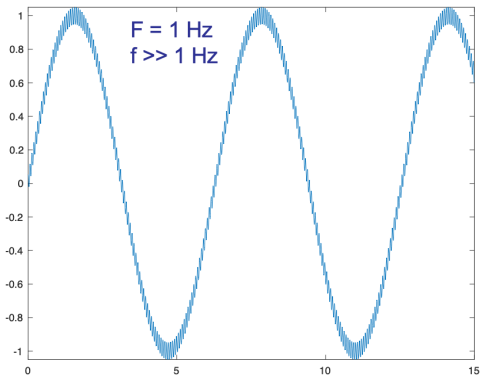

Figure 6.1: The module of current source for dynamic conductance measurements. The signal with higher frequency (¿1) is locked by a lock-in amplifier.

dation and contamination can cause difficulty for distinguishing the SC features from the tunneling spectra.

6.2 Methods

6.2.1 Scanning Tunneling Microscopy

The tunneling conductance of Bi2212 have been reported through various experimental methods. Scanning tunneling microscopy (STM) was employed to reveal the surface electronic structure through vacuum tunneling in which vacuum acts as the high-potential barrier. if a normal-metal tip was used during the STM experiments, the spectra indicate the superconductor-insulator-normal metal (SIN) tunneling. The background conductance also accounts for the results, and the measured spectra need to be calibrated [67, 68]. Some studies characterized the SC order parameters of HTS with a conventional SC tip such as lead through superconductor-insulator-superconductor (SIS) tunneling [69, 70]. These

studies have resolved the quasiparticles coherence peaks and observed the spectral inhomogeneities point-to-point on the a-b plane surfaces because STM probes the density of states along the c-axis.

The cleaved planes of Bi2212 are mostly along the bismuth-oxide (Bi-O) layers which are only weakly bonded with the Van der Waals forces. Therefore, the SC copper-oxide (Cu-O) planes are buried underneath the non-metallic Bi-O planes in the STM experimental setup. The SC characteristics are not acquired directly through transport on the SC a-b planes, but through the non-metallic layers along the c-axis. Therefore, STM is beneficial to resolve the density of states spatially, but it is not the ideal tool to solve the pairing symmetry of SC order parameters.

6.2.2 Point-Contact Junctions

Point contact junctions are also a common geometry to acquire the tunneling conductance spectra [47]. However, it is difficult to differentiate the contribution from the a-b plane tunneling and the c-axis tunneling since the contacts penetrate through the tested materials. In contrast, break-junctions hold the advantage of isolating the a-b plane tunneling from c-axis tunneling by the cleaving directions [71].

6.2.3 Break-Junctions

Break-junctions hold the advantage of isolating the a-b plane tunneling from c-axis tunneling by the cleaving directions. As mentioned earlier, Bi2212 is a two-dimensional SC material that can be exfoliated between the Bi-O planes with a normal vector parallel to the c-axis. Hence, both tunneling along with the a-b plane and c-axis can be measured

depending on the cleaving orientation in this way. However, the preparation processes for break-junction conductance measurements makes it difficult to control the barrier orientations on the a-b plane. The cleavage needs to be performed under vacuum for the a-b plane tunneling. The previous studies [71] have shown the a-b plane of Bi2212 is sensitive to the environment, and no well-developed junctions can be achieved if cleavage happens under atmosphere.

As mentioned earlier, Bi2212 is a two-dimensional SC material that can be exfoliated between the Bi-O planes with a normal vector parallel to the c-axis. Hence, both tunneling along with the a-b plane and c-axis can be measured depending on the cleaving orientation in this way. However, the preparation processes for break-junction conductance measurements makes it difficult to control the barrier orientations on the a-b plane. The cleavage needs to be performed under vacuum for the a-b plane tunneling. The previous studies have shown the a-b plane of Bi2212 is sensitive to the environment, and no well-developed junctions can be achieved if cleavage happens under atmosphere.

6.3 Challenges for HTS

One of the challenges to study cuprate HTS thin films is the film quality. Most cuprate thin films exhibit grain boundaries, detwinning, and mismatches with the substrates. The non-uniformity may partially contribute to the ambiguity of SC characteristics and the the spatially inhomogeneous energy spectra of HTS thin films. Although the quality of cuprate films have been optimized and the root mean square roughness has been reduced from 10 nm in average down to 4 nm, the roughness value is still much higher than

a thin-film-like exfoliated single crystals. As a single-crystalline cuprate HTS, Bi2212 is known to have atomically flat surfaces after cleavage with average roughness around 1 nm, and thus can be a good platform to study the SC characteristics in the energy spectra of cuprate HTS with such uniformity.

6.4 Tunneling Spectra with Bi2212 He-FIB Barriers

To perform tunneling conductance measurements, a highly resistive barrier is needed to limit the amount of current at high-voltage regions to observe the full spectrum. If the current values hit the intrinsic critical currents, it will activate the Josephson tunneling between the layers along the c-axis and the characteristics will appear in the tunneling spectrum. The first intrinsic I-V branches usually show up at around 1 mA. Therefore, to focus on the quasiparticle tunneling through the a-b plane transport excluding c-axis Josephson tunneling, we want to be able to enter the normal state of the a-b plane junction and observe the gap-like features below the critical currents of intrinsic junctions. We trimmed down the 4-um (w = 4 um) SIS junction down to 0.4 um (w' = 0.4 um) with He-FIB to make the barrier more resistive. Here comes another advantage of He-FIB, post-modification. We followed the trimming traces of the junction (w = 4 um) from the sides of the crystals and further extend them to the center. The I-V characteristics of the junction were thus altered by changing the junction width (w). The value of Ic at 4.2K was decreased from 20 uA to 250 nA, and the value of Rn was increased from 8 ohms to 500 ohms after the post-modification. This is around 60 80 times difference in their I-V characteristics with 10 times smaller junction area. The changes are not proportional to

the modified junction size. We suggest this is due to extra disordered regions created by extending the insulating traces. The modified junction (w' = 0.4 um) is more resistive and has a barrier with higher potential after processing.

We add a smaller modulation with higher frequency (2k Hz) onto the sweeping 1-Hz main signal for measuring I-V. The differential conductance results are measured by locking the small modulation and dividing the differential current by differential voltage. The SC characteristics can be observed clearly in the spectrum with the gap-like features and the peak of supercurrent at zero voltage. STM studies have demonstrated that only a junction with good quality allows the investigation for the tunneling conductance of the pristine materials without uncertainties from the junctions. If the tunneling experiment is done with a contaminated junction, the SC characteristics can become unclear due to the leakage current from contamination in STM experiments. In our results, the SC features such as the supercurrent peak at zero bias and the gap-like features, are obviously investigated, and hence it is persuasive that the barriers are well-established in junctions made by He-FIB.

We have found our results agree with the previous works using break-junctions. The spectra appear gapless similarly with non-zero states between two peaks at the local maxima on both voltage sides. This is not rare in other experiments by directly probing the a-b plane conductance of cuprate HTS. Although the curves of the excitation spectra are nothing resembling the BCS model, the temperature dependency of the gap-like features falls into prediction of the BCS theory. We define half of the distance between the two local maxima in the conductance spectra as the order parameter of the SC gap. The black

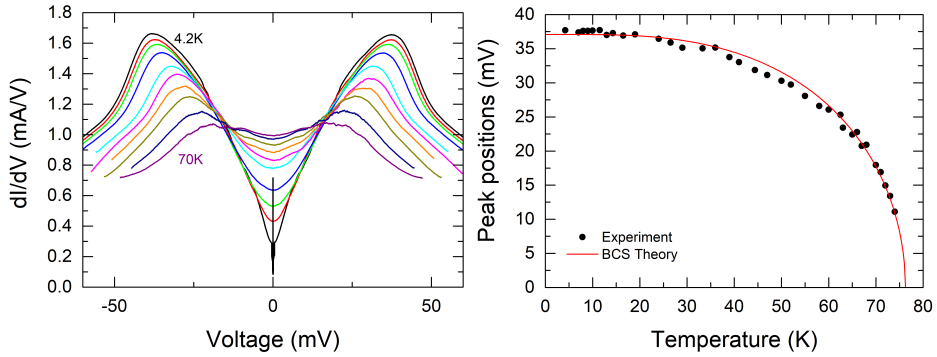

Figure 6.2: The temperature dependent differential conductance measurements

data points are acquired from the serial measurements of tunneling conductance within a temperature range from 4.2 K to 74 K. The curves for 72 K and 74 K are not presented in the differential conductance results for clarity. We calculated the constant of 2delta/kT to be around 5, which is deviated from the typical value for conventional superconductors 3.52. The V-shape spectra between the two local maximum are mostly considered as the evidence for the anisotropic d-wave component in HTS because of the presences of the nodes and lobes. However, we also found our results follow the BCS model in the temperature dependency of differential conductance, which may suggest contribution from the isotopic s-wave component. Further investigation on angular dependency of the gap-like features can provide another perspective for pairing symmetry, and this is achievable with the He-FIB technique we used in this work.

In conclusion, we have demonstrated the plane tunneling conductance measurement are achievable with He-FIB junctions to study quasiparticles excitation spectrum on the a-b plane of single-crystalline Bi2212. The I-V characteristics of He-FIB junctions can be tuned by the fabrication parameters such as ion doses and defined sizes. The orientation

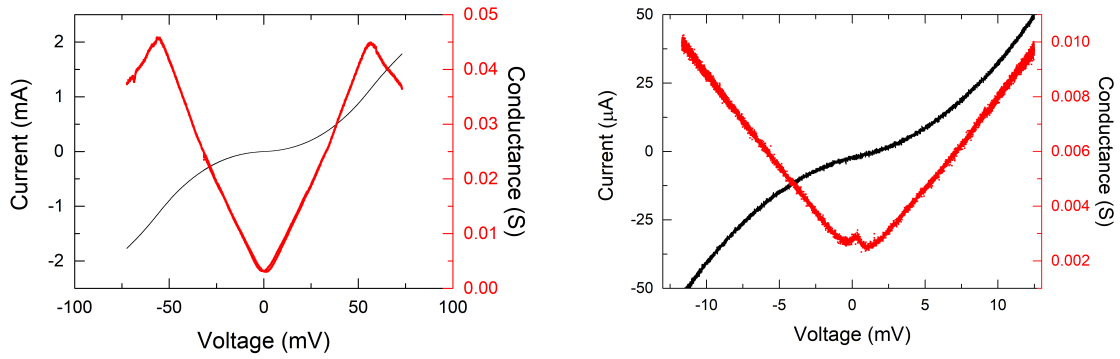

Figure 6.3: The tunneling experiment done with a Bi-2212 extremely resistive barrier instead of a Josephson junction.

of the He-FIB junctions is confirmed to be on the a-b plane by magnetic field modulation with Fraunhofer-like diffraction patterns. Another benefit to have a-b plane junctions is to allow three-dimensional SC circuit designs if one can incorporate them with the c-axis intrinsic junctions of Bi2212. The metal-insulator-transition is observed in the He-FIB junctions of Bi2212 with strengthening the barrier potential. The quasiparticle a-b plane tunneling are directly probed by HTS, and the clear superconducting features shown in the spectrum point out the good quality of the barrier in the a-b plane He-FIB Bi2212 junction. Although the spectra themselves don't resemble the BCS behaviors, the temperature tendency of the defined gap parameters can be well predicted with the BCS model. Our study on the angular experiments of differential conductance of Bi2212 single crystals using He-FIB junctions are expected in near future.

Another attempt of the differential conductance measurement gave us a different gap-like feature with wider distance between two peaks. The orientation of the tunneling barrier on the cleaved Bi-2212 crystal may be the reason for different gap values. The

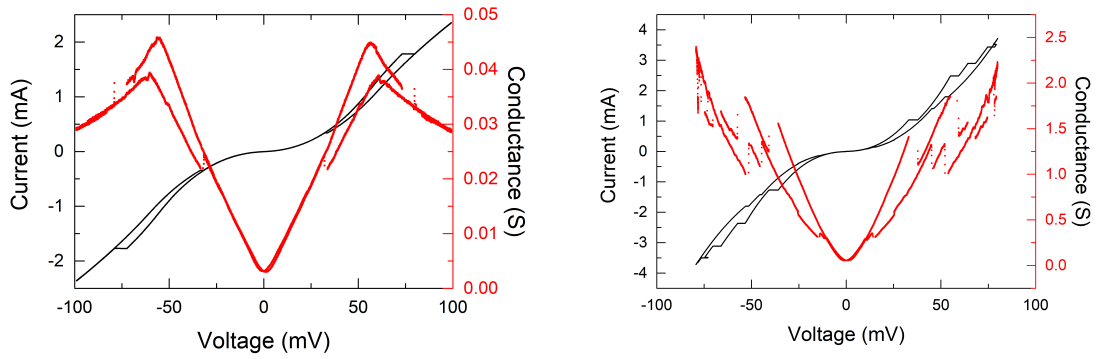

Figure 6.4: The tunneling experiment done with a Bi-2212 weak barrier that hits the intrinsic critical current steps.

central peak of supercurrent was very weak and only could be observed within a smaller voltage range, which may be caused by extra ion damage that made the device a resistor instead of a junction.

If the barrier is not resistive enough, the effect of intrinsic junctions can be seen on the results of differential conductance. The branches-like structures will also appear in dIdV at the same voltage position in I-V.

Chapter 7

Conclusions

The technique using a focused helium ion beam (He-FIB) for Josephson junctions fabrication has been applied to the cuprate thin films of $YBa_2Cu_3O_{7-\delta}$ (YBCO) and the cuprate single crystals of $Bi_2Sr_2CaCu_2O_{8+\delta}$ (Bi-2212). The orientations of junctions fabricated in this way are in-plane with the *a*-*b* planes, that is, in-plane with the superconducting copper-oxide planes. The first *a*-*b* plane Bi-2212 junction was successfully made with helium ion irradiation. The junction parameters were analyzed and discussed with different variables such as ion doses, junction widths, and thickness of cleaved Bi-2212 crystals. The junction orientations were confirmed by applying an external magnetic field along the *c*-axis and the Fraunhofer patters formed by modulated critical currents were investigated. By studying the barrier strenth through the *I*-*V* characteristics, the metal-insulator-transition of barriers was found in both YBCO thin films and Bi-2212 single crystals.

The tunneling experiments were measured through a direct tunneling between two homogeneous high-transition-temperature superconductors (HTS) across a He-FIB barrier.

Tunneling through the He-FIB barriers allows investigations for both Josephson tunneling and quasi-particles tunneling. The sharp peak at the zero bias voltage in the tunneling spectra demonstrates the supercurrent from cooper pairs tunneling. The full range of quasi-particles excitation spectra can be observed in the high voltage regimes. The V-shaped spectra of YBCO and Bi-2212 both show the gapless behaviors, which intrigues the speculations of d-wave component. The distances between the two local maximum in the spectra are defined as the gap-like features. In the temperature dependent measurements, the temperature dependence of the gap-like features can be fitted with the Bardeen–Cooper–Schrieffer theory model. The fitting result revealed a depressed T_C around 76 K, which is lower than the R-T result, due to the input current exceeding the current density of materials.

The detailed Bi-2212 He-FIB junction parameters are reported in this dissertation, and the report can assist the further advancement of three-dimensional superconducting circuit designs with the intrinsic Josephson junctions of Bi-2212. The mechanisms of cuprate HTS was slightly peeked from the results of tunneling experiments on the Bi-2212 cleaved single crystals. To further understand the pairing symmetry, angular tunneling experiments with Bi-2212 single crystals can be further proceeded with He-FIB with its advantage of flexible abilities to place the a-b plane junctions at any desired angles.

Bibliography

[1] S Martin, Anthony T Fiory, RM Fleming, LF Schneemeyer, and Joseph V Waszczak. Temperature dependence of the resistivity tensor in superconducting bi 2 sr 2.2 ca 0.8 cu 2 o 8 crystals. *Physical review letters*, 60(21):2194, 1988.

[2] Y Kotaka, T Kimura, H Ikata, J Shimoyama, K Kitazawa, K Yamafuji, K Kishio, and D Pooke. Doping state and transport anisotropy in bi2212 single crystals. *Physica C: Superconductivity*, 235:1529–1530, 1994.

[3] EA Ekimov, VA Sidorov, ED Bauer, NN Mel'Nik, NJ Curro, JD Thompson, and SM Stishov. Superconductivity in diamond. *nature*, 428(6982):542–545, 2004.

[4] Brian David Josephson. Possible new effects in superconductive tunnelling. *Physics letters*, 1(7):251–253, 1962.

[5] Shane A Cybart, EY Cho, TJ Wong, Björn H Wehlin, Meng K Ma, Chuong Huynh, and RC Dynes. Nano josephson superconducting tunnel junctions in yba 2 cu 3 o 7–δ directly patterned with a focused helium ion beam. *Nature nanotechnology*, 10(7):598–602, 2015.

[6] Vinay Ambegaokar and Alexis Baratoff. Tunneling between superconductors. *Physical Review Letters*, 10(11):486, 1963.

[7] WC Stewart. Current-voltage characteristics of josephson junctions. *Applied physics letters*, 12(8):277–280, 1968.

[8] DE McCumber. Effect of ac impedance on dc voltage-current characteristics of superconductor weak-link junctions. *Journal of Applied Physics*, 39(7):3113–3118, 1968.

[9] Peter A Rosenthal, MR Beasley, K Char, MS Colclough, and G Zaharchuk. Flux focusing effects in planar thin-film grain-boundary josephson junctions. *Applied physics letters*, 59(26):3482–3484, 1991.

[10] Shota Suzuki, Hiroki Taniguchi, Tsukasa Kawakami, Maxen Cosset-Cheneau, Tomonori Arakawa, Shigeki Miyasaka, Setsuko Tajima, Yasuhiro Niimi, and Kensuke Kobayashi. Electrical contacts to thin layers of $Bi_2Sr_2CaCu_2O_{8+\delta}$. *Applied Physics Express*, 11(5):053201, 2018.

[11] Maw-Kuen Wu, Jo R Ashburn, ClJ Torng, Ph H Hor, Rl L Meng, Lo Gao, Z Jo Huang, YQ Wang, and aCW Chu. Superconductivity at 93 k in a new mixed-phase y-ba-cu-o compound system at ambient pressure. *Physical review letters*, 58(9):908, 1987.

[12] Paola Benzi, Elena Bottizzo, and Nicoletta Rizzi. Oxygen determination from cell dimensions in ybco superconductors. *Journal of Crystal Growth*, 269(2-4):625–629, 2004.

[13] Stephen McCoy. *Rare Earth Cuprate Analysis for High Tc Superconducting Devices*. University of California, Riverside, 2020.

[14] Yan-Ting Wang, Robert Semerad, Stephen J McCoy, Han Cai, Jay LeFebvre, Holly Grezdo, Ethan Y Cho, Hao Li, and Shane A Cybart. Ybco-ceo2-ybco multilayers grown by reactive co-evaporation on sapphire wafers. *IEEE Transactions on Applied Superconductivity*, 29(5):1–4, 2019.

[15] James F Ziegler and Jochen P Biersack. The stopping and range of ions in matter. In *Treatise on heavy-ion science*, pages 93–129. Springer, 1985.

[16] Hiroshi Maeda, Yoshiaki Tanaka, Masao Fukutomi, and Toshihisa Asano. A new high-tc oxide superconductor without a rare earth element. *Japanese Journal of Applied Physics*, 27(2A):L209, 1988.

[17] C Michel, M Hervieu, MM Borel, A Grandin, F Deslandes, Ja Provost, and B Raveau. Superconductivity in the bi-sr-cu-o system. *Zeitschrift für Physik B Condensed Matter*, 68(4):421–423, 1987.

[18] J Zhao and Mohindar S Seehra. Dependence of tc of bi2sr2cacu2o8+ x on high temperature cycling and oxygen stoichiometry. *Physica C: Superconductivity*, 159(5):639–642, 1989.

[19] WA Groen and DM De Leeuw. Oxygen content, lattice constants and tc of bi2sr2cacu2o8+ δ. *Physica C: Superconductivity*, 159(4):417–421, 1989.

[20] B Khaykovich, E Zeldov, D Majer, TW Li, PH Kes, and M Konczykowski. Vortex-lattice phase transitions in bi 2 sr 2 cacu 2 o 8 crystals with different oxygen stoichiometry. *Physical review letters*, 76(14):2555, 1996.

[21] MR Presland, JL Tallon, RG Buckley, RS Liu, and NE Flower. General trends in oxygen stoichiometry effects on tc in bi and tl superconductors. *Physica C: Superconductivity*, 176(1-3):95–105, 1991.

[22] M Runde, JL Routbort, SJ Rothman, KC Goretta, JN Mundy, X Xu, and JE Baker. Tracer diffusion of oxygen in bi 2 sr 2 cacu 2 o x. *Physical Review B*, 45(13):7375, 1992.

[23] TW Li, PH Kes, WT Fu, AA Menovsky, and JJM Franse. Anisotropic oxygen diffusion in bi2sr2cacu2o8+ x single crystals. *Physica C: Superconductivity*, 224(1-2):110–116, 1994.

[24] T Watanabe, T Fujii, and A Matsuda. Anisotropic resistivities of precisely oxygen controlled single-crystal bi 2 sr 2 cacu 2 o 8+ δ: Systematic study on"spin gap"effect. *Physical review letters*, 79(11):2113, 1997.

[25] Jean-Marie Tarascon, Y Le Page, P Barboux, BG Bagley, LH Greene, WR McKinnon, GW Hull, M_ Giroud, and DM Hwang. Crystal substructure and physical properties of the superconducting phase bi 4 (s r, c a) 6 cu 4 o 1 6+ x. *Physical Review B*, 37(16):9382, 1988.

[26] Robert M Hazen, CT Prewitt, RJ Angel, NL Ross, LW Finger, CG Hadidiacos, DR Veblen, Peter J Heaney, PH Hor, RL Meng, et al. Superconductivity in the high-t c bi-ca-sr-cu-o system: Phase identification. *Physical review letters*, 60(12):1174, 1988.

[27] MA Subramanian, CC Torardi, JC Calabrese, J Gopalakrishnan, KJ Morrissey, TR Askew, RB Flippen, U Chowdhry, and AW Sleight. A new high-temperature superconductor: Bi2sr3-x cax cu2o8+ y. *Science*, 239(4843):1015–1017, 1988.

[28] SA Sunshine, T Siegrist, LF Schneemeyer, DW Murphy, RJ Cava, B Batlogg, RB Van Dover, RM Fleming, SH Glarum, Sb Nakahara, et al. Structure and physical properties of single crystals of the 84-k superconductor bi 2.2 sr 2 ca 0.8 cu 2 o 8+ δ. *Physical Review B*, 38(1):893, 1988.

[29] JL Tallon, RG Buckley, PW Gilberd, MR Presland, IWM Brown, ME Bowden, LA Christian, and R Goguel. High-t c superconducting phases in the series bi 2.1 (ca, sr) n+ l cu n o 2n+ 4+ δ. *Nature*, 333(6169):153–156, 1988.

[30] Shozo Ikeda, Hideki Ichinose, Takashi Kimura, Takehiko Matsumoto, Hiroshi Maeda, Yoichi Ishida, and Keiichi Ogawa. Transmission electron microscope studies of intergrowth in bisrcacu2ox and high-tc superconducting phase. *Japanese journal of applied physics*, 27(6A):L999, 1988.

[31] Keikichi Nakamura, Junichi Sato, Masatsugu Kaise, and Keiichi Ogawa. Synthesis of artificially layered bi-sr-ca-cu oxide films and their thermal stability. *Japanese Journal of Applied Physics*, 28(3A):L437, 1989.

[32] Keikichi Nakamura, Junichi Sato, and Keiichi Ogawa. Formation of thermally stable multilayered bscco films with 2223, 2234 and 2245 structures. *Japanese journal of applied physics*, 29(1A):L77, 1990.

[33] MD Kirk, CB Eom, B Oh, SR Spielman, MR Beasley, A Kapitulnik, TH Geballe, and CF Quate. Scanning tunneling microscopy of the a-b planes of bi2 (ca, sr) 3cu2o8+ δ single crystal and thin film. *Applied physics letters*, 52(24):2071–2073, 1988.

[34] SH Pan, EW Hudson, J Ma, and JC Davis. Imaging and identification of atomic planes of cleaved bi 2 sr 2 cacu 2 o 8+ δ by high resolution scanning tunneling microscopy. *Applied physics letters*, 73(1):58–60, 1998.

[35] TM Shaw, SA Shivashankar, SJ La Placa, JJ Cuomo, TR McGuire, RA Roy, KH Kelleher, and DS Yee. Incommensurate structure in the bi-sr-ca-cu-o 80-k superconductor. *Physical Review B*, 37(16):9856, 1988.

[36] T Jacobs, S Sridhar, Qiang Li, GD Gu, and N Koshizuka. In-plane and cˆ-axis microwave penetration depth of bi 2 sr 2 ca 1 cu 2 o 8+ δ crystals. *Physical review letters*, 75(24):4516, 1995.

[37] Shih-Fu Lee, DC Morgan, RJ Ormeno, DM Broun, RA Doyle, JR Waldram, and K Kadowaki. a- b plane microwave surface impedance of a high-quality b i 2 s r 2 cac u 2 o 8 single crystal. *Physical review letters*, 77(4):735, 1996.

[38] JR Cooper, L Forro, and B Keszeit. Direct evidence for a very large penetration depth in superconducting bi 2 sr 2 cacu 2 o 8 single crystals. *Nature*, 343(6257):444–446, 1990.

[39] S Martin, AT Fiory, RM Fleming, GP Espinosa, and AS Cooper. Vortex-pair excitation near the superconducting transition of bi 2 sr 2 ca cu 2 o 8 crystals. *Physical review letters*, 62(6):677, 1989.

[40] A Schilling, F Hulliger, and HR Ott. In-plane london penetration depths near the critical temperature of tl 2 ba 2 ca n- 1 cu n o 2n+ 4 and (bi, pb) 2 sr 2 ca n- 1 cu n o 2n+ 4 (n= 2, 3). *Zeitschrift für Physik B Condensed Matter*, 82(1):9–13, 1991.

[41] VG Kogan, M Ledvij, A Yu Simonov, JH Cho, and DC Johnston. Role of vortex fluctuations in determining superconducting parameters from magnetization data for layered superconductors. *Physical review letters*, 70(12):1870, 1993.

[42] TTM Palstra, Bertram Batlogg, LF Schneemeyer, RB Van Dover, and Joseph V Waszczak. Angular dependence of the upper critical field of bi 2.2 sr 2 ca 0.8 cu 2 o 8+ δ. *Physical Review B*, 38(7):5102, 1988.

[43] Bertram Batlogg, TTM Palstra, LF Schneemeyer, Robert B Van Dover, and Robert J Cava. Superconducting and normal state parameters of bi2. 2sr2ca0. 8cu2o8+ δ single crystals: A comparison with ba2ycu3o7. *Physica C: Superconductivity*, 153:1062–1066, 1988.

[44] MJ Naughton, RC Yu, PK Davies, JE Fischer, RV Chamberlin, ZZ Wang, TW Jing, Nai Phuan Ong, and PM Chaikin. Orientational anisotropy of the upper critical field in single-crystal y ba 2 cu 3 o 7 and bi 2.2 ca sr 1.9 cu 2 o 8+ x. *Physical Review B*, 38(13):9280, 1988.

[45] AM Bykov, VN Korenivski, AN Ul'yanov, and Ya I Yuzhelevskii. Magnetocaloric effect and main parameters of bi2sr2ca2cu3oy textured ceramic superconductor. *Physica C: Superconductivity and its Applications*, 193(1-2):25–32, 1992.

[46] P Mandal, A Poddar, AN Das, B Ghosh, and Pranab Choudhury. Excess conductivity and thermally activated dissipation studies in bi2sr2ca1cu2ox single crystals. *Physica C: Superconductivity*, 169(1-2):43–49, 1990.

[47] A Plecenik, M Grajcar, Š Beňačka, P Seidel, and A Pfuch. Finite-quasiparticle-lifetime effects in the differential conductance of bi 2 sr 2 cacu 2 o y/au junctions. *Physical Review B*, 49(14):10016, 1994.

[48] T Matsushita. Effect of short coherence length along the c-axis on the irreversibility line in high-tc superconductors. *Physica C: Superconductivity*, 205(3-4):289–295, 1993.

[49] WE Lawrence and S Doniach. Theory of layer-structure superconductors. In *pp 361-2 of Proceedings of the Twelfth International Conference on Low Temperature Physics./Kanda, E.(ed.). Tokyo Keigaku Publishing Co., Ltd.(1971).* Stanford Univ., Calif., 1971.

[50] LG Aslamazov and AI Larkin. The influence of fluctuations on the properties of a superconductor at temperatures higher than critical. *Fiz. Tverd. Tela [Sov. Phys. Solid State 10, 875 (1968)]*, 10(1104):87, 1968.

[51] R Kleiner, F Steinmeyer, G Kunkel, and P Müller. Intrinsic josephson effects in $Bi_2Sr_2CaCu_2O_8$ single crystals. *Physical review letters*, 68(15):2394, 1992.

[52] R Kleiner and P Müller. Intrinsic josephson effects in high-t c superconductors. *Physical Review B*, 49(2):1327, 1994.

[53] D Drung, R Cantor, M Peters, HJ Scheer, and HAPF Koch. Low-noise high-speed dc superconducting quantum interference device magnetometer with simplified feedback electronics. *Applied physics letters*, 57(4):406–408, 1990.

[54] Lutfi Ozyuzer, Alexei E Koshelev, Cihan Kurter, Nachappa Gopalsami, Qiang Li, Masashi Tachiki, Kazuo Kadowaki, Takashi Yamamoto, Hidetoshi Minami, Hiroshi Yamaguchi, et al. Emission of coherent thz radiation from superconductors. *Science*, 318(5854):1291–1293, 2007.

[55] Michel H Devoret and Robert J Schoelkopf. Superconducting circuits for quantum information: an outlook. *Science*, 339(6124):1169–1174, 2013.

[56] Ulrich Welp, Kazuo Kadowaki, and Reinhold Kleiner. Superconducting emitters of thz radiation. *Nature Photonics*, 7(9):702–710, 2013.

[57] EY Cho, MK Ma, Chuong Huynh, K Pratt, DN Paulson, VN Glyantsev, RC Dynes, and Shane A Cybart. Yba2cu3o7- δ superconducting quantum interference devices with metallic to insulating barriers written with a focused helium ion beam. *Applied physics letters*, 106(25):252601, 2015.

[58] Hao Li, Han Cai, Ethan Y Cho, Stephen J McCoy, Yan-Ting Wang, Jay C LeFebvre, Yuchao W Zhou, and Shane A Cybart. High-transition-temperature nanoscale superconducting quantum interference devices directly written with a focused helium ion beam. *Applied Physics Letters*, 116(7):070601, 2020.

[59] S Matsui, H Matsutera, T Yoshitake, and T Satoh. Radiation damage effects in ion-implanted bi-sr-ca-cu-o superconducting thin films. *Applied physics letters*, 53(21):2096–2098, 1988.

[60] Takeo Aruga, Saburo Takamura, Taiji Hoshiya, and Mamoru Kobiyama. Effects of he ion irradiation on superconductivity of bi-sr-ca-cu-o films. *Japanese journal of applied physics*, 28(6A):L964, 1989.

[61] Yan-Ting Wang, Jay C LeFebvre, Ethan Y Cho, Stephen J McCoy, Hao Li, Genda Gu, Kazuo Kadowaki, and Shane A Cybart. Fabrication of bi _{2} sr _{2} cacu _{2} o _{8+x} ab-plane josephson junctions by a focused helium ion beam. *IEEE Transactions on Applied Superconductivity*, 31(5):1–4, 2021.

[62] T Mochiku and K Kadowaki. Growth and properties of bi2sr2 (ca, y) cu2o8+ δ single crystals. *Physica C: Superconductivity*, 235:523–524, 1994.

[63] T Mochiku, K Hirata, and K Kadowaki. Crystallinity improvement of $Bi_2Sr_2CaCu_2O_{8+\delta}$ single crystal by tsfz method. *Physica C: Superconductivity*, 282:475–476, 1997.

[64] GD Gu, K Takamuku, N Koshizuka, and S Tanaka. Large single crystal bi-2212 along the c-axis prepared by floating zone method. *Journal of Crystal growth*, 130(1-2):325–329, 1993.

[65] Katsuyoshi Hotta, Toshimasa Suzuki, Haruo Hirose, Hidekazu Magome, and Kazuhiro Endo. Bi-Pb-Sr-Ca-Cu-O superconductor properties with water-included organic solvent. *Journal of the Japan Society of Powder and Powder Metallurgy*, 38(8):1062–1065, 1991.

[66] Richard Livengood, Shida Tan, Yuval Greenzweig, John Notte, and Shawn McVey. Subsurface damage from helium ions as a function of dose, beam energy, and dose rate. *Journal of Vacuum Science & Technology B: Microelectronics and Nanometer Structures Processing, Measurement, and Phenomena*, 27(6):3244–3249, 2009.

[67] Ch Renner et al. Vacuum tunneling spectroscopy and asymmetric density of states of bi 2 sr 2 cacu 2 o 8+ δ. *Physical Review B*, 51(14):9208, 1995.

[68] Ch Renner, Bernard Revaz, K Kadowaki, Ivan Maggio-Aprile, and Ø Fischer. Observation of the low temperature pseudogap in the vortex cores of bi 2 sr 2 cacu 2 o 8+ δ. *Physical Review Letters*, 80(16):3606, 1998.

[69] Hikari Kimura, RP Barber Jr, Shimpei Ono, Yoichi Ando, and Robert C Dynes. Scanning josephson tunneling microscopy of single-crystal bi 2 sr 2 cacu 2 o 8+ δ with a conventional superconducting tip. *Physical review letters*, 101(3):037002, 2008.

[70] Hikari Kimura, RP Barber Jr, S Ono, Yoichi Ando, and RC Dynes. Josephson scanning tunneling microscopy: A local and direct probe of the superconducting order parameter. *Physical Review B*, 80(14):144506, 2009.

[71] D Mandrus, J Hartge, C Kendziora, L Mihaly, and L Forro. Gapless superconductivity in bi2sr2cacu2o8. *EPL (Europhysics Letters)*, 22(3):199, 1993.